1 **Title:** Production of Neoproterozoic banded iron formations in a partially ice-covered ocean

2 **Authors:** Kaushal Gianchandani[1]*, Itay Halevy[2]*, Hezi Gildor[1], Yosef Ashkenazy[3], Eli
3 Tziperman[4]

4 **Affiliations:**

5 [1]Fredy & Nadine Herrmann Institute of Earth Sciences, Hebrew University of Jerusalem,
6 Jerusalem, Israel

7 [2]Department of Earth and Planetary Sciences, Weizmann Institute of Science, Rehovot, Israel

8 [3]Blaustein Institutes for Desert Research, Ben-Gurion University of the Negev, Midreshet Ben-
9 Gurion, Israel

10 [4]Department of Earth and Planetary Sciences and School of Engineering and Applied Sciences,
11 Harvard University, Cambridge, MA, USA

12 *Corresponding author. Email: kaushal.g@mail.huji.ac.il (KG), itay.halevy@weizmann.ac.il (IH)

13 **Abstract:**

14 Neoproterozoic snowball Earth events challenge our understanding of the climate system.
15 Specifically, it is debated whether the oceans were completely ice-covered ('hard' snowball) or
16 whether the tropical ocean was ice-free ('soft' snowball), with implications for interpretations of
17 the geochemical record and the survival of photosynthetic life. Banded iron formations associated
18 with the older and longer Sturtian glaciation are considered evidence for a hard snowball, in which
19 Fe^{2+} accumulated in the anoxic ocean interior. Here, using a state-of-the-art ocean model including
20 representation of thick sea glaciers and Neoproterozoic biogeochemistry, we find that ocean
21 circulation in a soft snowball yields iron deposition at the interface between ferruginous and
22 oxygenated water masses, in spatial patterns that agree with the observed distribution of Sturtian
23 banded iron formations.

24 **Main Text:**

25 Banded iron formations (BIFs) are iron- and silica-rich sedimentary rocks, the genesis of which is
26 thought to require low oceanic O_2 concentrations, in agreement with their occurrence before ~1800
27 million years ago (Ma), when Earth's oceans are proposed to have been anoxic[1,2]. An exception to
28 this pattern of occurrence, Neoproterozoic (1000–541 Ma) iron formations were deposited when
29 atmospheric O_2 levels were 1–10% of today's[3]. Neoproterozoic BIFs occur in association with the
30 earlier and longer of two low-latitude glaciations, the so-called 'snowball Earth' events[4–7], in
31 which the ocean and continents are suggested to have been ice-covered for tens of millions of
32 years[8,9]. Widespread sedimentary and geochemical evidence supports the occurrence of the
33 Neoproterozoic pan-glacials, though the exact nature of these events, including the meridional
34 extent of marine ice is still debated. The Neoproterozoic BIFs have been suggested to support a
35 'hard' snowball[4,5], in which pole-to-pole ice cover renders the ocean anoxic, allowing the
36 accumulation of ferrous iron (Fe^{2+}). Although viable explanations for the survival of the
37 photosynthesis-based marine biosphere through a hard snowball have been proposed[10], such an
38 extreme climate poses a serious challenge to life[5]. Alternatively, a 'soft' snowball[7] with tropical
39 swaths of open water does not pose a similar challenge to the biosphere, but O_2 input to the ocean

40   by air-sea gas exchange may have prevented the mobility of Fe^{2+} required for widespread
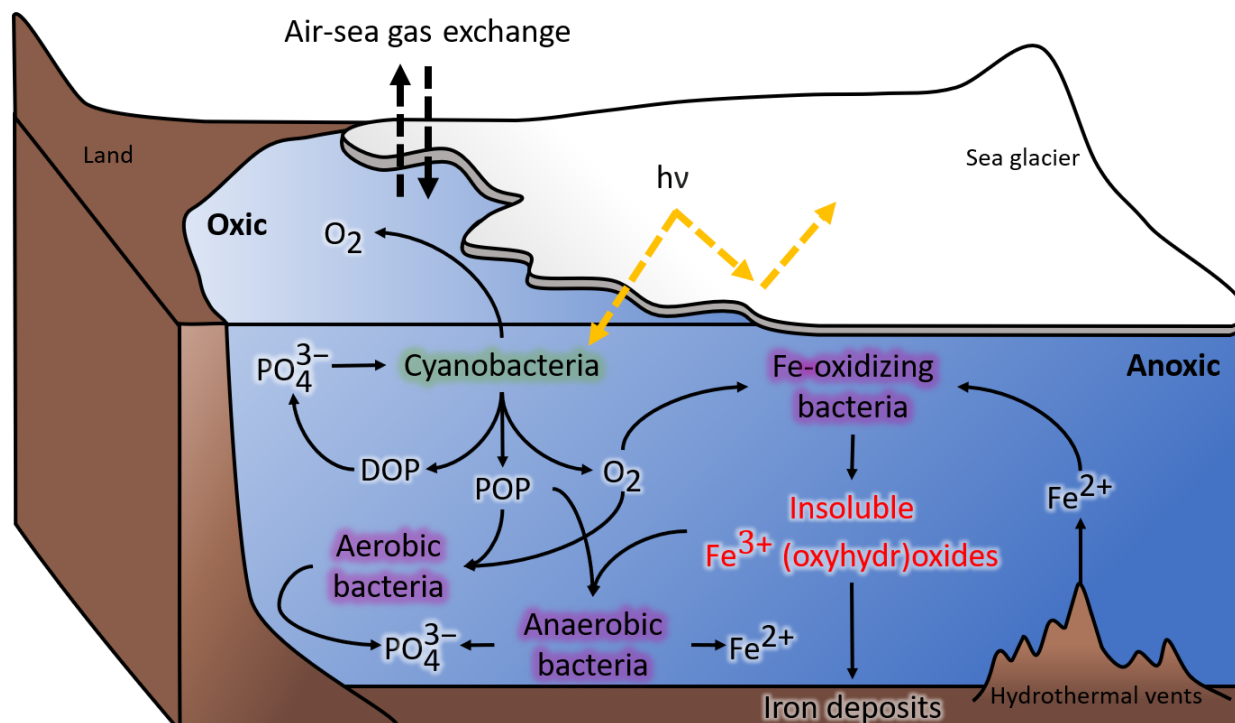41   deposition of BIFs[10,11].

Fig. 1. Schematic representation of the biogeochemical model. Cyanobacteria, limited by low
seawater $[PO_4^{3-}]$, produce organic matter (dissolved organic phosphorus, DOP and particulate
organic phosphorus, POP) and O_2 in ice-free regions. Aerobic respiration of the organic matter
consumes some of the O_2, as do Fe^{2+}-oxidizing bacteria, which produce Fe^{3+} oxides. The fraction
of Fe^{3+} oxides that is not used by anaerobic bacteria to remineralize organic matter settles to the
seabed, forming iron deposits.

42   We revisit the notion that BIFs cannot precipitate under soft snowball conditions using a state-of-
43   the-art ocean general circulation model (GCM), which includes the representation of thick sea
44   glaciers that extend to a prescribed latitude and a new biogeochemical model tailored to the
45   Neoproterozoic (Fig. 1; see Methods and Supplementary Information, SI, for details). In the model
46   biogeochemical iron cycle, a hydrothermal source of Fe^{2+} (estimated to be 0.36 Tmol y^{-1}, SI) at
47   mid-oceanic ridges is balanced by oxidation and deposition of ferric iron (Fe^{3+}) oxides, which
48   occurs where Fe^{2+}-bearing waters meet oxygenated waters. The location of such reaction and
49   deposition fronts depends on the transport of Fe^{2+} and O_2 from their hydrothermal and
50   photosynthetic sources, respectively. Patterns of phosphate concentration ($[PO_4^{3-}]$) and $[O_2]$
51   obtained in an idealized model configuration (SI) with a 100% modern $[PO_4^{3-}]$ and a stoichiometry
52   of organic matter oxidation (O_2 consumed to P released) representative of modern marine organic
53   matter are consistent with today's ocean (Fig. S1), and atmospheric O_2 stabilizes at ~62% present
54   atmospheric levels.

55   Previous ocean-atmosphere-cryosphere modelling efforts have identified multiple stable climate
56   states in which ice-free ocean exists equatorward of latitudes between 60° and 5°[11,12]. Accordingly,
57   we examined a completely ice-free ocean and partially glaciated oceans in which the ice-free

58 region extended from 30°S to 30°N and 12°S to 12°N. The size of the marine PO_4^{3-} pool during
59 snowball Earth episodes is unknown, though several factors lead to expectations of lower-than-
60 present seawater $[PO_4^{3-}]$. These include low continental weathering rates, photosynthetic carbon
61 fixation and nutrient uptake during the glacial advance and in regions of open water, limited
62 organic matter remineralization in a partly ice-covered ocean, and PO_4^{3-} adsorption onto iron
63 oxides in an ocean with relatively high Fe^{2+} concentrations. Hence, we examined iron deposition
64 patterns at 100%, 10%, 3% and 1% the mean present-day seawater $[PO_4^{3-}]$ (3 µM), the lower three
65 of which are within the proposed range required to sustain low Proterozoic atmospheric O_2
66 levels[13,14], and consistent with low Proterozoic primary productivity[15]. With these parameter
67 combinations, cases in which 90% or more of the iron deposited within the model grid points
68 corresponding to the hydrothermal Fe^{2+} sources were considered less viable for BIF deposition on
69 multiple continental margins, as suggested by the sedimentary record[10].

70 We first discuss the ocean's circulation at the three ice-cover extents considered here. The depth-
71 averaged velocity field (the barotropic flow) in the ice-free ocean (Fig. S2A) indicates the presence
72 of a strong eastward zonal jet (~10 cm s^{-1}) in the northern high latitudes. The flow everywhere
73 else in the ocean is much weaker (~1 cm s^{-1}), especially in the young ocean basins formed during
74 the breakup of the supercontinent Rodinia (~0.1 cm s^{-1}). The barotropic flow in the ocean weakens
75 with an increase in the ice cover, particularly at the high latitudes (Fig. S2B-C). The meridional
76 overturning circulation in the ice-free case is predominantly driven by sinking of cold water in the
77 southern high latitudes and upwelling everywhere else (Fig. S2D). An increase in the extent of ice
78 cover modifies the overturning patterns drastically, and in contrast to the ice-free ocean, the
79 circulation in both the 30°S to 30°N and 12°S to 12°N ice-free region cases is most intense in the
80 equatorial region near the ocean surface (Fig. S2E-F).

81 The zonally averaged $[O_2]$ distributions vary with the extent of the ice-free region (Fig. 2A-C). As
82 an example, when the mean seawater $[PO_4^{3-}]$ is 3% present-day, the mean $[O_2]$ in the ocean is 1.6
83 µM, 4.7 µM and 17 µM in the 12°S to 12°N ocean, 30°S to 30°N ocean and the completely ice-
84 free ocean, respectively, which is ~hundred-fold lower than today, due to limitation of primary
85 productivity by the low PO_4^{3-} levels. In an ice-free ocean, the mean $[Fe^{2+}]$ is ~0.01 nM and Fe^{2+} is
86 restricted to the vicinity of the hydrothermal ridges (Fig. 2D). However, the low $[O_2]$ in the
87 partially glaciated oceans allows Fe^{2+} build-up, with a $[Fe^{2+}]$ range of 0 to >1000 nM, and a mean
88 of 4.8 nM and 4 nM for the snowballs with an ice-free region from 12°S to 12°N and 30°S to 30°N,
89 respectively (Fig. 2E-F). With the model $[Fe^{2+}]$ and $[O_2]$ fields, we compared model iron
90 deposition rates and spatial patterns with estimates based on Neoproterozoic BIFs. To this end, we
91 compiled reports of Sturtian BIFs[16–21] and used the fractional concentration of hematite in the
92 samples, their density, thickness and the approximate deposition duration to conservatively
93 estimate that iron deposition rates during the Sturtian glaciation were between ~0.003 and ~0.4
94 mol m^{-2} y^{-1} (SI). The distributions of model iron deposition rates show precipitation away from
95 the hydrothermal sources that is within the range of calculated BIF deposition rates for the 12°S
96 to 12°N ocean and 30°S to 30°N ocean, when the mean $[PO_4^{3-}]$ is 1–10% of today's (Figs. 2H-I,
97 S3H-I and S4H-I). We note that this model consistency with the observations is achieved at $[Fe^{2+}]$
98 ~two orders of magnitude lower than previously thought to be required for widespread
99 Neoproterozoic BIF deposition[22,23]. Thus, we suggest that Fe^{2+} supply and mobility, not
100 concentration, are the actual requirements for widespread BIF deposition, in the Neoproterozoic
101 and over Earth history in general. At modern mean seawater $[PO_4^{3-}]$, most of the ocean interior is

102   oxygenated, and >95% of the iron oxide precipitation occurs only in the model grid points
103   corresponding to the hydrothermal Fe^{2+} sources (Figs. 3A and S5G-I).
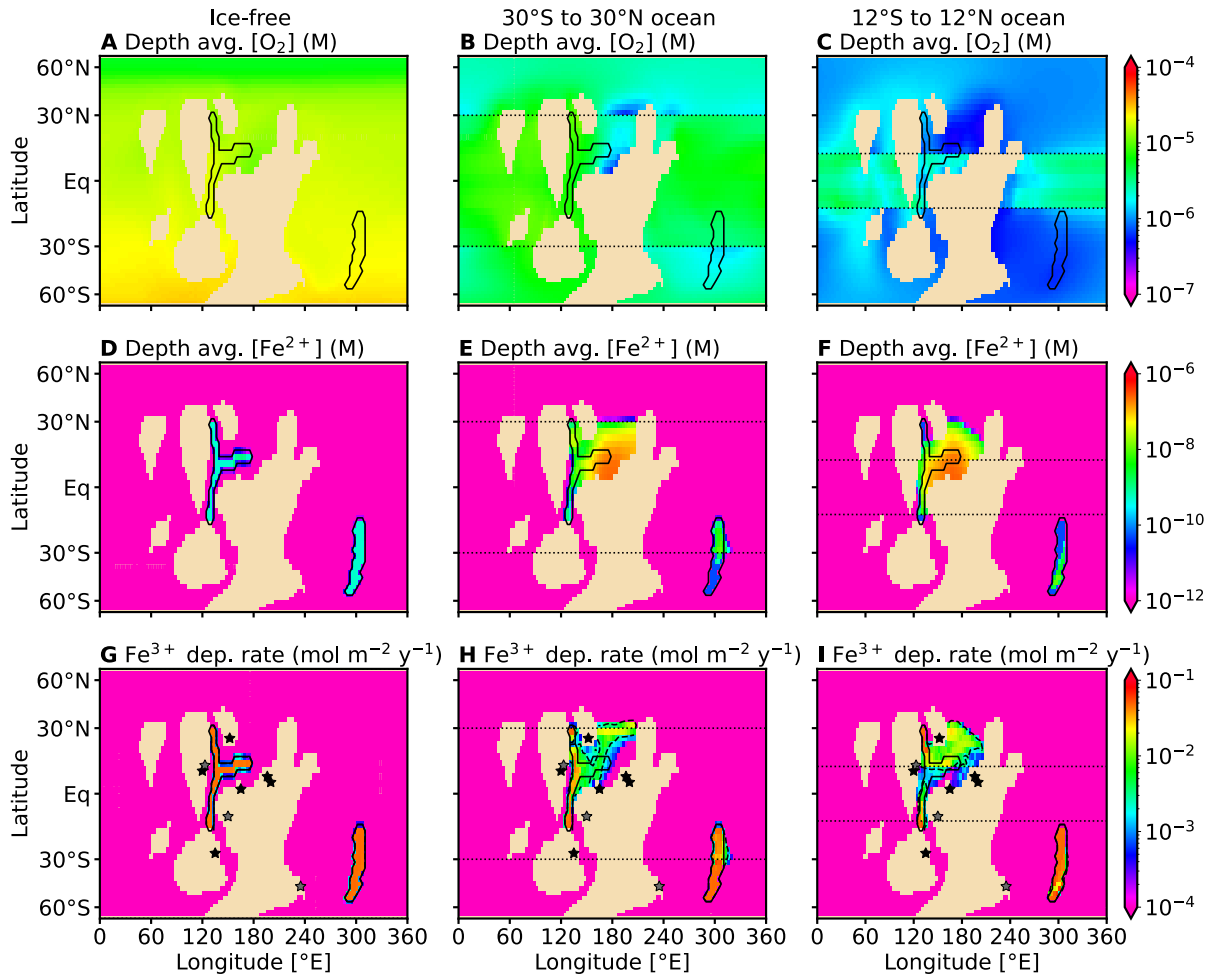

Fig. 2. Results of the 3D ocean model with a mean seawater $[PO_4^{3-}]$ of 0.1 μM (3% modern). (**A**)-(**C**) Depth-averaged distribution of $[O_2]$ and (**D**)-(**F**) $[Fe^{2+}]$ and the (**G**)-(**I**) spatial distribution of iron deposition rates in snowballs with different meridional extents of sea glaciers. Iron deposition rates are calculated by vertical integration of net Fe^{2+} oxidation profiles. The solid black contours mark the sites of hydrothermal Fe^{2+} injection, based on estimated locations of mid-oceanic ridges. The dotted black horizontal lines denote the extent of the ice-free region. The dashed black lines in (**G**)-(**I**) enclose the region where iron deposition rates are within the range estimated from Neoproterozoic BIFs. The stars indicate the approximate location of BIFs associated with the Sturtian pan-glacial. BIFs denoted by the gray stars have been excluded from the estimation of BIF deposition rate (SI).

104   Multiple BIF deposition sites emerge in the simulations with 1-10% modern $[PO_4^{3-}]$ (Figs. 2H-I,
105   S3H-I and S4H-I), several of which are located in the deep ocean away from the continents. BIFs
106   deposited at these deep sites are unlikely to be preserved, in contrast with the BIFs deposited on
107   the continental margins facing the young ocean basins that formed during the breakup of Rodinia.
108   This is consistent with the clustering of all but one of the BIFs dated to the Sturtian pan-glacial

109 around these young ocean basins. The paleogeographic reconstruction does not resolve inland seas,
110 which host some of the Neoproterozoic BIFs, but we postulate that iron deposition is expected also
111 in such seas that were connected to the basins represented in the model (e.g., apparent inland BIF
112 locations in Fig. 2G-I). To assess the agreement between iron deposition patterns obtained in
113 different simulations with the spatial distribution of Neoproterozoic BIFs, we calculated the
114 fraction of the continental margin area in the vicinity of approximate BIF locations [Fig. S6, Ref.
115 [10,24,25]] where model iron deposition rates are within the range inferred from the compilation of
116 Sturtian BIFs.

117 Our simulations show that the spatial pattern
118 of iron precipitation is sensitive to both the
119 extent of ice cover and the mean seawater
120 [PO_4^{3-}]. For example, at 3% modern [PO_4^{3-}]
121 levels, reaction fronts between O_2-bearing
122 and Fe^{2+}-bearing water masses result in a
123 spatial distribution of iron oxidation and
124 deposition such that ~18% of continental
125 margins under consideration are viable for
126 precipitation of BIFs in the snowballs with
127 30°S to 30°N and 12°S to 12°N ice-free
128 ocean, while practically none (<3%) of the
129 margins are found to be suitable for
130 precipitation of BIFs in the ice-free case (Fig.
131 3B). More generally, in simulations with
132 mean seawater [PO_4^{3-}] between 1% and 10%
133 modern levels, O_2-bearing and Fe^{2+}-bearing
134 water masses meet in the vicinity of Sturtian
135 BIFs for the two partially ice-covered oceans
136 considered. However, neither the ice-free
137 ocean nor the partially ice-covered oceans
138 show an affinity for precipitation of BIFs at
139 modern [PO_4^{3-}] levels, and all of the Fe^{2+} is
140 deposited close to the hydrothermal source
141 (Fig. 3A and Fig. S5G-I). These results
142 suggest that iron deposition patterns and
143 rates consistent with the Sturtian BIFs can be
144 obtained in partially ice-covered oceans with
145 lower-than-present seawater [PO_4^{3-}] (<~10%
146 modern levels). Due to model uncertainties,
147 we stop short of attempting to identify the
148 precise [PO_4^{3-}] levels and meridional ice
149 extent that yield the most consistent iron
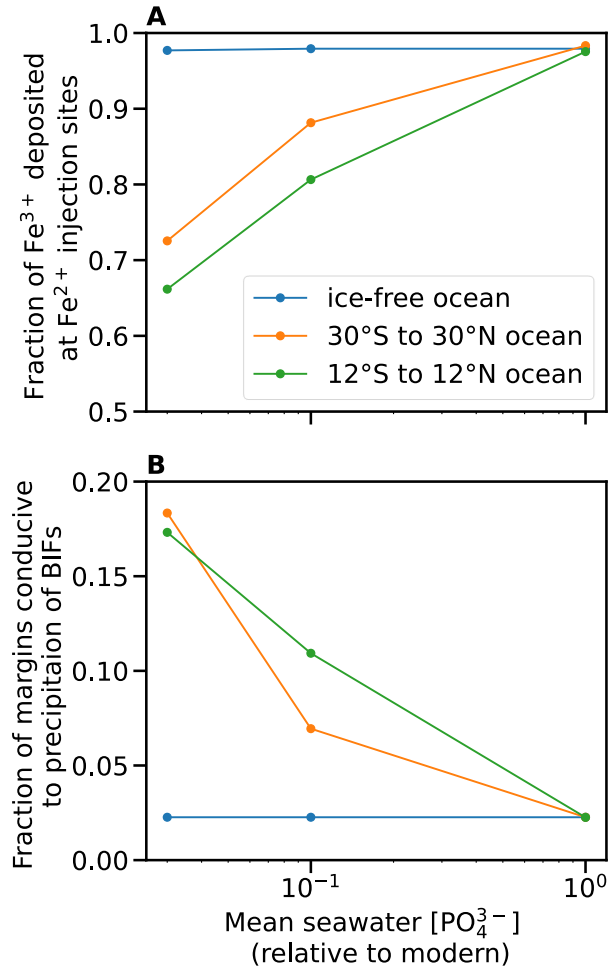150 deposition patterns.

Fig. 3. (A) Fraction of Fe^{3+} deposited at the Fe^{2+} injection site. (B) Fraction of continental margins in the vicinity of Sturtian BIFs that are viable for model precipitation of BIFs.

151 Climate models of different degrees of complexity show that Earth's climate can exhibit both soft
152 and hard snowball states[11,26–28]. Perturbation of the soft snowball state in existing climate models
153 leads to deglaciation or full glaciation (hard snowball)[29]. Nevertheless, evidence of a productive
154 and diverse marine ecosystem during both pan-glacials, which would be challenging to achieve
155 under hard snowball conditions, warrants a critical examination of the soft snowball's viability[10].

156 The hard snowball state[27,28,30,31] is suggested to have led to an anoxic ocean interior in which
157 dissolved Fe^{2+} accumulated, to be oxidized and deposited only in spatially limited regions where
158 O_2 was available, such as the interface between anoxic seawater and oxygenated meltwater plumes
159 near the ice grounding line[10,32]. Under such a scenario, precipitation of iron oxides and production
160 of BIFs is expected on all glaciated continental margins[10], in contrast with the occurrence of
161 Neoproterozoic BIFs only on some continental margins (Fig. 2G-I). Our analysis shows that a
162 phosphate-deficient ocean is conducive to production of BIFs for different extents of marine ice-
163 cover, wherever Fe^{2+}-bearing and oxygenated water masses meet. We find several combinations
164 of $[PO_4^{3-}]$ and marine ice-cover that predict BIF deposition at multiple sites, including on the
165 continental margins facing the young ocean basins that formed during the fragmentation of
166 Rodinia, consistent with the observed distribution of Sturtian BIFs (Figs. 2H-I, S3H-I and S4H-I).
167 Though we cannot predict the meridional extent of marine ice cover with the present model, our
168 findings prompt investigations of the plausibility of a soft snowball state in more complete climate
169 models, which include atmosphere-ocean-cryosphere coupling and a realistic continental
170 configuration. Lastly, our findings highlight the role of Fe^{2+} fluxes into, and mobility within,
171 Earth's oceans as the necessary conditions for widespread BIF deposition. In contrast with
172 previous suggestions, a high Fe^{2+} concentration is found unnecessary.

173

174 **References:**
175 1. Bekker, A. *et al.* Iron Formation: The Sedimentary Product of a Complex Interplay among
176   Mantle, Tectonic, Oceanic, and Biospheric Processes*. *Economic Geology* **105**, 467–508
177   (2010).
178 2. Konhauser, K. O. *et al.* Iron formations: A global record of Neoarchaean to
179   Palaeoproterozoic environmental history. *Earth Sci Rev* **172**, 140–177 (2017).
180 3. Lyons, T. W., Reinhard, C. T. & Planavsky, N. J. The rise of oxygen in Earth's early
181   ocean and atmosphere. *Nature* **506**, 307–315 (2014).
182 4. Kirschvink, J. L. Late Proterozoic low-latitude global glaciation: the snowball Earth. *The
183   Proterozoic Biosphere* **52**, 51–52 (1992).
184 5. Hoffman, P. F., Kaufman, A. J., Halverson, G. P. & Schrag, D. P. A neoproterozoic
185   snowball earth. *Science (1979)* **281**, 1342–1346 (1998).
186 6. Evans, D. A. D. Stratigraphic, geochronological, and paleomagnetic constraints upon the
187   Neoproterozoic climatic paradox. *Am J Sci* **300**, 347–433 (2000).
188 7. Hyde, W. T., Crowley, T. J., Baum, S. K. & Peltier, W. R. Neoproterozoic 'snowball
189   Earth' simulations with a coupled climate/ice-sheet model. *Nature* **405**, 425–429 (2000).
190 8. Nelson, L. L. *et al.* Geochronological constraints on Neoproterozoic rifting and onset of
191   the Marinoan glaciation from the Kingston Peak Formation in Death Valley , California (
192   USA). **48**, 1083–1087 (2020).
193 9. Rooney, A. D., Yang, C., Condon, D. J., Zhu, M. & Macdonald, F. A. U-Pb and Re-Os
194   geochronology tracks stratigraphic condensation in the Sturtian snowball Earth aftermath.
195   *Geology* **48**, 625–629 (2020).
196 10. Hoffman, P. F. *et al.* Snowball Earth climate dynamics and Cryogenian geology-
197   geobiology. *Sci Adv* **3**, (2017).
198 11. Abbot, D. S., Voigt, A. & Koll, D. The Jormungand global climate state and implications
199   for Neoproterozoic glaciations. *J Geophys Res* **116**, D18103 (2011).
200 12. Yang, J., Peltier, W. R. & Hu, Y. The Initiation of Modern "Soft Snowball" and "Hard
201   Snowball" Climates in CCSM3. Part II: Climate Dynamic Feedbacks. *J Clim* **25**, 2737–
202   2754 (2012).

203 13. Laakso, T. A. & Schrag, D. P. Regulation of atmospheric oxygen during the Proterozoic.
204 *Earth Planet Sci Lett* **388**, 81–91 (2014).
205 14. Laakso, T. A. & Schrag, D. P. A theory of atmospheric oxygen. *Geobiology* **15**, 366–384
206 (2017).
207 15. Crockford, P. W. *et al.* Triple oxygen isotope evidence for limited mid-Proterozoic
208 primary productivity. *Nature* **559**, 613–616 (2018).
209 16. Klein, C. & Beukes, N. J. Sedimentology and geochemistry of the glaciogenic late
210 Proterozoic Rapitan iron-formation in Canada. *Economic Geology* **88**, 542–565 (1993).
211 17. Macdonald, F. A. & Cohen, P. A. Chapter 35 The Tatonduk inlier, Alaska–Yukon border.
212 *Geological Society, London, Memoirs* **36**, 389–396 (2011).
213 18. Lechte, M. A., Wallace, M. W., Hood, A. van S. & Planavsky, N. Cryogenian iron
214 formations in the glaciogenic Kingston Peak Formation, California. *Precambrian Res* **310**,
215 443–462 (2018).
216 19. Feng, L., Huang, J., Lu, D. & Zhang, Q. Major and trace element geochemistry of the
217 Neoproterozoic syn-glacial Fulu iron formation, South China. *Geol Mag* **154**, 1371–1380
218 (2017).
219 20. Lottermoser, B. G. & Ashley, P. M. Geochemistry, petrology and origin of
220 Neoproterozoic ironstones in the eastern part of the Adelaide Geosyncline, South
221 Australia. *Precambrian Res* **101**, 49–67 (2000).
222 21. Lechte, M. A., Wallace, M. W. & Hoffmann, K.-H. Glacio-marine iron formation
223 deposition in a *c.* 700 Ma glaciated margin: insights from the Chuos Formation, Namibia.
224 *Geological Society, London, Special Publications* **475**, 9–34 (2019).
225 22. Chan, C. S., Emerson, D. & Luther, G. W. The role of microaerophilic Fe-oxidizing
226 micro-organisms in producing banded iron formations. *Geobiology* **14**, 509–528 (2016).
227 23. Song, H. *et al.* The onset of widespread marine red beds and the evolution of ferruginous
228 oceans. *Nat Commun* **8**, (2017).
229 24. Hoffman, P. F. & Li, Z. X. A palaeogeographic context for Neoproterozoic glaciation.
230 *Palaeogeogr Palaeoclimatol Palaeoecol* **277**, 158–172 (2009).
231 25. Cox, G. M. *et al.* Neoproterozoic iron formation: An evaluation of its temporal,
232 environmental and tectonic significance. *Chem Geol* **362**, 232–249 (2013).
233 26. Pollard, D. Snowball Earth: A thin-ice solution with flowing sea glaciers. *J Geophys Res*
234 **110**, C07010 (2005).
235 27. Yang, J., Peltier, W. R. & Hu, Y. The initiation of modern soft and hard Snowball Earth
236 climates in CCSM4. *Climate of the Past* **8**, 907–918 (2012).
237 28. Ashkenazy, Y. *et al.* Dynamics of a Snowball Earth ocean. *Nature* **495**, 90–93 (2013).
238 29. Pierrehumbert, R. T., Abbot, D. S., Voigt, A. & Koll, D. Climate of the neoproterozoic.
239 *Annu Rev Earth Planet Sci* **39**, 417–460 (2011).
240 30. Ashkenazy, Y., Gildor, H., Losch, M. & Tziperman, E. Ocean Circulation under Globally
241 Glaciated Snowball Earth Conditions: Steady-State Solutions. *J Phys Oceanogr* **44**, 24–43
242 (2014).
243 31. Ashkenazy, Y. & Tziperman, E. Variability, Instabilities, and Eddies in a Snowball
244 Ocean. *J Clim* **29**, 869–888 (2016).
245 32. Lechte, M. A. *et al.* Subglacial meltwater supported aerobic marine habitats during
246 Snowball Earth. *Proceedings of the National Academy of Sciences* **116**, 25478–25483
247 (2019).
248
249

Methods:

Ocean

We use the Massachusetts Institute of Technology General Circulation Model (MITgcm)[33] to perform the simulations discussed in this study. The MITgcm is a free, open-source, general circulation model in which a finite volume method is implemented to solve the equations of fluid motion (i.e., momentum equations, continuity equation, and diffusion equations of temperature and salinity and equation of state). We employ the full equation of state provided in the MITgcm, MDJWF[34], and make the hydrostatic and Boussinesq approximations. The model uses a spherical grid spanning 72°S to 72°N with a resolution of 3° in latitude and has 37 vertical levels spanning a depth of 3000 m (height of vertical levels from the surface to the bottom: 10 m, 12 m, 16 m, 20 m, 25 m, 32 m, 40 m, 50 m, 60 m, 75 m, 80 m, 2 levels × 90 m, and 24 levels × 100 m). The longitudinal resolution is 3° as well, with 20 grid points in the idealized box configuration simulations and 120 grid points in the Neoproterozoic simulations. Unresolved eddies in the ocean are parameterized using the Gent-McWilliams/Redi (GM-Redi) scheme[35,36], and the background diffusion coefficient is set to 1000 $m^2\ s^{-1}$. The lateral and vertical viscosities are set to $5 \times 10^5\ m^2\ s^{-1}$ and $10^{-3}\ m^2\ s^{-1}$, and the vertical diffusivity and implicit vertical diffusivity for convection are set to $10^{-4}\ m^2\ s^{-1}$ and $10\ m^2\ s^{-1}$. We also use a nondimensional grid-dependent biharmonic viscosity of 0.1 to suppress the grid-scale noise. The vertical diffusivity for biogeochemical variables is set to $3 \times 10^{-5}\ m^2\ s^{-1}$. The third-order direct space-time flux limiter advection scheme (no. 33) is used for both momentum tracers and biogeochemical variables. The flat bathymetry ocean is subjected to a constant geothermal heat flux of 0.1 W m^{-2} [37]. At the surface, the ocean is forced by a zonal wind stress that changes for the different meridional extent of the sea glaciers. The wind stress field for the idealized box configuration simulations is similar to the present-day, and for ice-free Neoproterozoic simulation is the zonally averaged wind stress obtained from fully coupled ocean-atmosphere simulation of Cambrian-Precambrian boundary[38]. The wind stress fields for our snowball simulation conditions (spatial grid and ice opening) are generated by setting the wind stress over the ice-covered region to zero and using zonally averaged wind stress profiles over the ice-free region that are based on results from simulations of partially glaciated climate states carried out on fully coupled general circulation models[39,40]. The temperature at the surface (z = 0 m) is restored to temperature fields that are also generated on the basis of coupled model results[11,12]. Fig. S7A-B show the zonally-averaged restoration temperature and wind stress over the ocean for different meridional extents of sea glaciers. Fig. S7C shows the evaporation minus precipitation (E–P) fields over the ocean in the box simulations and in the Neoproterozoic ice-free simulations, these idealized E–P fields are generated by introducing a small asymmetry to the E–P field described in Ref. [41]. In both the snowballs, melting under the sea glaciers is balanced by evaporation in the ice-free region, which conserves the mean salinity of the ocean.

Sea glaciers

Given the uncertainties regarding the thickness of ice during the Neoproterozoic glaciations, we estimate ice thickness using a simplified energy balance. A similar calculation has been used to estimate the thickness of ice on Jupiter's moon Europa[42]. We begin by assuming that a constant geothermal flux of 0.1 W m^{-2} is applied to the ocean bottom and that the component of tidal heating in both the ice and ocean is negligible. Moreover, the temperature within the ice varies linearly with depth. In this case, the thickness of ice is given by:

$$h \ = \ \rho_i c_{p,i} \kappa \frac{T_f - T_i}{Q},$$

296

297 where ρ_i is the density, $c_{p,i}$ is the heat capacity and κ is the temperature diffusion constant of ice.
298 T_f and T_i are the freezing and surface temperature of the ice, and Q is the internal heat flux (the
299 geothermal heat flux). T_f is a function of temperature and salinity:

300 $$T_f = 273.16 + 0.0901 - 0.0575 \times S - 7.61 \times 10^{-8} \times P_b,$$

301

302 where S is the salinity and $P_b = \rho_i g h$ is the pressure at the bottom of the ice. The gradient in solar
303 insolation yields a gradient in the surface temperature of the ice, and in turn, a gradient in ice
304 thickness. This gradient in ice thickness causes it to flow smoothly, thereby partially relaxing the
305 gradient[43]. Hence, we approximate the thickness of the ice as the meridional average of h
306 calculated using the prescribed temperature field. Under these assumptions, the ice thickness can
307 iteratively be estimated as:

308 $$\langle h \rangle_{j+1} = \rho_i c_{p,i} \kappa \frac{\langle T_f \rangle_j - \langle T_i \rangle}{Q}.$$

309

310 The algorithm[42], when initialized from the typical seawater freezing temperature of 271 K and the
311 surface temperature fields such as the ones given in Ref. [11,12], predicts a certain ice thickness,
312 which implies a certain P_b value and a modified freezing temperature. For the temperature fields
313 shown in Fig. S7A, the ice thickness converges to 490 m and 253 m below the sea surface within
314 a few iterations for snowballs with 12°S to 12°N ice-free ocean and 30°S to 30°N ice-free ocean,
315 respectively. To avoid any numerical artifacts that may arise from partially filled grid-cells, we
316 use a thickness of 510 m and 265 m below the sea surface for the snowballs with 12°S to 12°N
317 ocean and 30°S to 30°N ocean respectively. The effect of this sea glacier is simulated using the
318 SHELFICE package[44]. Unlike the SEAICE package, the SHELFICE package in the MITgcm can
319 handle a thick sea glacier spanning over multiple vertical levels, which makes it better suited to
320 snowball Earth modeling.

321

322 **Biogeochemical cycle**
323 The biogeochemical model presented here is based on Refs. [45,46], implemented in the MITgcm
324 using a combination of the 'GCHEM' and 'DIC' packages.
325 (https://mitgcm.readthedocs.io/en/latest/phys_pkgs/phys_pkgs.html#biogeochemistry-packages).
326 MITgcm's biogeochemical setup (GCHEM+DIC), in its default configuration, considers coupled
327 cycles of carbon, oxygen, phosphorus and alkalinity. These cycles are expressed using five
328 variables that do not affect the physical circulation: dissolved inorganic carbon (DIC), alkalinity
329 (Alk), phosphate (PO_4^{3-}), dissolved organic phosphorus (DOP), and oxygen (O_2). The velocity
330 fields and eddy diffusivities calculated by the physical model are used to transport these
331 compounds, which are additionally produced and consumed locally by biogeochemical reactions,
332 as described below.

333

334 For this study, we focus on the phosphorus and oxygen cycles. Additionally, we incorporate an
335 iron (Fe^{2+}) cycle and a well-mixed atmospheric box to the pre-existing setup. The atmospheric box
336 only keeps track of the total O_2 in the atmosphere. The values of all parameters described below
337 are provided in Table S1. The sources and sinks for each tracer are summarized below:

338 $$\frac{\partial}{\partial t}[PO_4^{3-}] = -J_{production} - \frac{\partial}{\partial z} F_P + \kappa_{remin}[DOP],$$

339 $$\frac{\partial}{\partial t}[DOP] = f_{DOP} J_{production} - \kappa_{remin}[DOP],$$

340 $$\frac{\partial}{\partial t}[O_2] = \frac{k_w}{\Delta z_{surf}}\left(\frac{n_{O_2}^{model\ atmosphere}}{n_{O_2}^{present-day}}[O_2]_{sat} - [O_2]_{surf}\right) + f([O_2]) \times \left(r_{O_2:P}\frac{\partial}{\partial t}[PO_4^{3-}]\right)$$

341 $$- k_{Fe}[Fe^{2+}],$$

342 $$\frac{\partial}{\partial t}[Fe^{2+}] = F_{Fe}^{hydrothermal} - k_{Fe}[Fe^{2+}] - \frac{\partial}{\partial z}F_{Fe}^{recycle},$$

343

344 where square brackets denote concentration, $J_{production}$ is primary production, $\frac{\partial}{\partial z}F_P$ is the partial

345 derivative with depth of the particulate organic phosphorus sinking flux, and κ_{remin} is the rate

346 constant of remineralization of DOP to PO_4^{3-}. The gas transfer velocity for O_2, is given by k_w and

347 Δz_{surf} is the thickness of the surface layer. The moles of O_2 in the model atmosphere and the

348 present-day atmosphere are given by $n_{O_2}^{model\ atmosphere}$ and $n_{O_2}^{present-day}$ respectively, and $[O_2]_{sat}$

349 and $[O_2]_{surf}$ are the saturation and surface concentration of O_2, respectively. The function

350 $f([O_2]) = 1$ for $[O_2] > 0$ and 0 otherwise. The number of moles of O_2 consumed to remineralize

351 1 mole of the typical Neoproterozoic marine biomass is given by: $- r_{O_2:P}$ (see below).

352

353 $F_{Fe}^{hydrothermal}$ is the hydrothermal influx of Fe^{2+} to the ocean, k_{Fe} is the oxidation rate of Fe^{2+} to

354 Fe^{3+}, which accounts for both abiotic and microbial pathways (described below), and $\frac{\partial}{\partial z}F_{Fe}^{recycle}$ is

355 the partial derivative with depth of the particulate Fe^{3+} sinking flux, which gives the rate at which

356 particulate Fe^{3+} is recycled back to Fe^{2+} by anaerobic remineralization of organic matter. The

357 tendency term for the number of moles of O_2 in the model atmosphere ($n_{O_2}^{model\ atmosphere}$) is:

358

359 $$\frac{d}{dt}n_{O_2}^{model\ atmosphere} = -\xi\left(k_w A_{surf}\left(\frac{n_{O_2}^{model\ atmosphere}}{n_{O_2}^{present-day}}[O_2]_{sat} - [O_2]_{surf}\right) - \Phi_{red}\right),$$

360

361 where, $\xi = 10^4$ is an arbitrary constant introduced to accelerate the convergence of the

362 atmospheric box to a steady state, A_{surf} is the area of the ocean surface, Φ_{red} is the (mole

363 equivalent) rate of consumption of O_2 required to balance the volcanic flux of reduced gases into

364 the atmosphere (e.g., SO_2, H_2S, CO, CH_4, H_2). Other oxygen sinks relevant to the present-day

365 Earth system, like oxidative weathering of the continents and respiration by the terrestrial

366 biosphere are considered negligible during a global glaciation.

367

368 $J_{production}$, which is a function of the light (L) and $[PO_4^{3-}]$, is given by:

369 $$J_{production} = \alpha\frac{L}{L + \kappa_L}\frac{[PO_4^{3-}]}{[PO_4^{3-}] + \kappa_{PO_4^{3-}}},$$

370

371 where κ_L and $\kappa_{PO_4^{3-}}$ are Michaelis-Menten-type half-saturation constants typical of ocean biology,

372 and α is the maximum community production. The expression for L is given by:

373 $$L = f_{PAR}Q_{SW} \times \exp(-kz),$$

374

375 where, f_{PAR} is the fraction of shortwave radiation (SW) available for photosynthesis and k is the

376 light attenuation constant. Since the light available for photosynthesis declines exponentially with

377 depth, most of the biological activity in the ocean is close to the surface. Primary production

converts a fraction of PO_4^{3-} to DOP (f_{DOP}), which can be advected by the physical circulation in the ocean, while the rest forms particulate organic phosphorus (POP), which sinks[47]. The downward sinking flux of POP is given by:

$$F_{POP} = \begin{cases} (1 - f_{DOP}) \int_0^{z_i} J_{production} \; dz & \text{if } z < z_c \\ (1 - f_{DOP}) \int_0^{z_c} J_{production} \; dz & \text{if } z \geq z_c \end{cases},$$

where z_i is a reference depth below which the downward flux of POP is calculated and z_c is the compensation depth. In present-day ocean models, POP is remineralized according to a power law relation related almost entirely to aerobic respiration[48]. Additionally, our model accounts for remineralization of POP by anaerobic microbes that reduce Fe^{3+} particles (see below).

As was previously mentioned, Fe^{2+} in the ocean can be oxidized by abiotic and microbial pathways, both O_2-related and light driven. The Fe^{2+} oxidation rate accounting for both abiotic and microbial processes is:

$$k_{Fe} = \frac{k_{Fe}^{ab}}{1 - f_{bio}},$$

where k_{Fe}^{ab} is the abiotic rate constant of oxidation and f_{bio} is the fraction of microbial Fe^{2+} oxidation out of the total oxidation as a function of available $[O_2]$[49]; k_{Fe}^{ab} is given by:

$$k_{Fe}^{ab} = k_1 [O_2][OH^-]^2$$
$$\log k_1 = 21.56 - \frac{1545}{T} - 3.29 \sqrt{I} + 1.52 \, I,$$

where T is the temperature (in Kelvins), $I = \frac{19.992 \, S}{10^3 - 1.005 \, S}$ and S is the salinity of seawater (48). The fraction of microbial Fe^{2+} oxidation is given by:

$$f_{bio} = 1.074 \times 10^{-3} \times \exp\left(\left(\frac{[O_2]}{K_H}\right)\right),$$

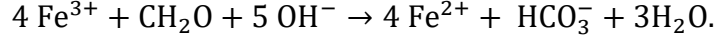where K_H is Henry's Law constant for O_2:

$$K_H = 1.3 \times 10^{-3} \times \exp\left(1500 \left(\frac{1}{T} - \frac{1}{298.15}\right)\right).$$

f_{bio} is capped at 0.95, an upper bound based on experimental results[49]. To allow model timesteps that are long enough so that convergence is reached over reasonable runtimes, chemical rate constants could not be too large. Thus, we prescribed an upper limit on k_{Fe} of 10^{-5} s^{-1}. This upper limit was applied wherever O_2 concentrations were high enough to result in k_{Fe} that was too large to allow efficient model timesteps, typically in the well oxygenated regions in the ocean (e.g., near the surface in the snowball with 12°S to 12°N ocean). The upper limit of k_{Fe} was prescribed in ~68% of the ocean volume in the snowball simulation with 12°S to 12°N ocean with 1% modern $[PO_4^{3-}]$, in >90% of the ocean volume for a lower ice-cover or higher $[PO_4^{3-}]$. The model results were relatively insensitive to this choice of an upper limit on k_{Fe} (Fig. S8).

415 The downward flux of Fe^{3+} produced from oxidation of Fe^{2+} is given by:

$$F_{Fe}^{down} = \int_0^{z_u} k_{Fe}[Fe^{2+}]\, dz,$$

417
418 where z_u is the reference up to which the downward flux of Fe^{3+} is calculated. We assume that a
419 fraction of sinking Fe^{3+} is preserved ($f_{preserved}$) while the rest is remineralized by anaerobic
420 microbes. This process restores some Fe^{2+} and is summarized by the following reaction:
421 $$4\,Fe^{3+} + CH_2O + 5\,OH^- \rightarrow 4\,Fe^{2+} + HCO_3^- + 3H_2O.$$
422
423 The anaerobic reduction of Fe^{3+} by bacteria follows Michaelis-Menten-type kinetics with respect
424 to the concentrations of both organic matter and Fe^{3+}:

$$\frac{d}{dt}[Fe^{3+}] = \mu \min\left(\frac{[Fe^{3+}]}{\kappa_{Fe} + [Fe^{3+}]}, \frac{[C]}{\kappa_C + [C]}\right),$$

426
427 where μ is the typical respiration rate, $[Fe^{3+}]$ and $[C]$ are the concentrations of Fe^{3+} and organic
428 matter respectively. The relevant half saturation constants for Fe^{3+} and C are κ_{Fe} and
429 κ_C respectively, and the smaller of the saturation terms is considered to limit the Fe^{3+} reduction
430 rate. Assuming a typical C:P ratio of 100:1 yields:

$$\frac{d}{dt}[Fe^{3+}] = \mu \min\left(\frac{[Fe^{3+}]}{\kappa_{Fe} + [Fe^{3+}]}, \frac{[POP]}{\kappa_C/100 + [POP]}\right),$$

433 and

$$\frac{d}{dt}[POP] = \frac{\mu}{400} \min\left(\frac{[Fe^{3+}]}{\kappa_{Fe} + [Fe^{3+}]}, \frac{[POP]}{\kappa_C/100 + [POP]}\right).$$

435
436 The factor of 400 comes from the Fe:C:P stoichiometry of the reaction. To calculate the flux of
437 recycled Fe^{3+} ($F_{Fe}^{recycle}$) and the effect of Fe^{3+} reduction on the vertical POP remineralization
438 profile, we further assume that $[POP]$ and $[Fe^{3+}]$ are proportional to F_P and F_{Fe}^{down} respectively.
439 If $F_{Fe}^{down} > (F_P/400)$, the fluxes of recycled Fe^{3+} and POP are given by:

$$F_P(z) = \begin{cases} F_{POP}\left(\dfrac{z}{z_i}\right)^{-\left(a_{remin} + \frac{\mu}{4\,\kappa_C \times a}\right)} & \text{if } F_P < w(z)\,(\kappa_C/100) \\[2ex] F_{POP}\left(\dfrac{z}{z_i}\right)^{-a_{remin}} & \text{otherwise} \end{cases},$$

441 and

$$F_{Fe}^{recycle}(z) = \left(1 - f_{preserved}\right)F_{Fe}^{down} - \mu\frac{F_P(z)}{w(z)\,(\kappa_C/100) + F_P(z)}.$$

443
444 Similarly, when $F_{Fe}^{down} < (F_P/400)$, the fluxes of recycled Fe^{3+} and POP are given by:

$$F_P(z) = F_{POP}\left(\frac{z}{z_i}\right)^{-a_{remin}},$$

446
447 and
448

449
$$F_{Fe}^{recycle}(z) = \begin{cases} (1 - f_{preserved})F_{Fe}^{down}\left(\dfrac{z}{z_i}\right)^{-\frac{\mu}{a\,\kappa_{Fe}}} & \text{if } F_{Fe}^{down} < w(z)\,\kappa_{Fe} \\ (1 - f_{preserved})F_{Fe}^{down} & \text{otherwise} \end{cases}.$$

450
451 Here, z_i is a reference depth below which the downward flux of POP is calculated (note that $z_i = $
452 z_c when $z > z_c$), a is the vertical gradient of particle sinking velocity such that $w(z) = az$ yields
453 the speed of the sinking particles at depth z, and a_{remin} is the exponent in Martin's curve for POP
454 remineralization in the modern ocean.

455
456 The Fe^{2+} influx to the ocean from axial and off-axis hydrothermal circulation depends on the Fe^{2+}
457 concentration in the fluid and the total water fluxes. The concentration of Fe^{2+} in axial and off-axis
458 hydrothermal fluids is estimated to be in the range $(0.75 - 6.5) \times 10^{-3}$ mol kg^{-1} and
459 $(0.4 - 6.0) \times 10^{-6}$ mol kg^{-1}, respectively[51–53]. Assuming that the Fe^{2+} concentration is uniformly
460 distributed in these ranges and the axial and off-axis water fluxes follow the distributions shown
461 in Ref. [54], we generated probability distributions corresponding to the axial and off-axis influx of
462 hydrothermal Fe^{2+} to the ocean (Fig. S9A-B). Separate from hydrothermal Fe^{2+} fluxes, weathering
463 of seafloor basalt can deliver Fe^{2+} to the ocean[55,56]. The Fe^{2+} flux from seafloor weathering is rather
464 difficult to constrain in the well-oxygenated modern ocean but it is estimated to be ~$0.1 - 0.3$ Tmol
465 y^{-1} and as high as 1.0 Tmol y^{-1} [57], though it is unclear that all the Fe^{2+} lost from the basalt actually
466 reaches the ocean. Given the existing estimates, we adopt a weathering Fe^{2+} flux uniformly
467 distributed between 0.1and 0.3 Tmol y^{-1} (Fig. S9C).

468
469 Convolving the distributions of axial and off-axis hydrothermal fluxes and seafloor weathering
470 flux yields a range of Fe^{2+} influxes between 0.2 and 0.67 Tmol y^{-1} (95% confidence interval) with
471 a mode of 0.36 Tmol y^{-1} (Fig. S9D). Though some have suggested higher hydrothermal fluxes in
472 Earth's deep past due to higher radiogenic heat production in the mantle[58], it remains unclear
473 whether the higher heat production led instead to more sluggish seafloor spreading[59] and a
474 hydrothermal flux similar to the Phanerozoic. We do not upscale the hydrothermal water flux,
475 leading to conservatively low Fe^{2+} influx estimates. Following the above analysis, we distribute
476 the mode Fe^{2+} influx of 0.36 Tmol y^{-1} on the model grid points corresponding to the suggested
477 locations of seafloor spreading centers during the Sturtian glaciation. Moreover, we do not taper
478 the Fe^{2+} influx with increasing distance from the spreading centers, since both near-axis and off-
479 axis hydrothermal inputs occur close to the spreading centers (considering the spatial resolution of
480 the ocean model), and the dissolved products of seafloor weathering are expected to reach the
481 ocean mostly where the sedimentary cover on the basaltic crust is thin to absent (i.e., near the
482 spreading centers).

483
484 The marine phytoplankton community during the Neoproterozoic primarily comprised of
485 cyanobacteria. Previous studies[60–63] show that the metabolite content of typical cyanobacterial
486 biomass is: 51% protein, 16% carbohydrates, 23% lipid and 10% nucleic acid which is slightly
487 different from the average composition of modern phytoplankton (which includes diatoms,
488 coccolithophores, dinoflagellates, and cyanobacteria): 54% protein, 26% carbohydrates, 16% lipid
489 and 4% nucleic acid[64]. Despite these differences in the metabolite content, the oxidation state of
490 cyanobacterial biomass is not significantly different from the gross modern assemblage (we
491 estimated < 1% variation in H:C$_{org}$ and < 10% variation in O:C$_{org}$ ratios), which suggests that the
492 difference between the Neoproterozoic and present-day O$_2$:P ratio is expected to arise from a
493 difference between the C:P ratios of cyanobacteria and the modern assemblage and not from the

494   difference in the carbon oxidation state. Using the mean C:N:P ratio of 152:25:1 for
495   cyanobacteria[65], we calculate the following elemental composition of typical Neoproterozoic
496   plankton: $C_{152}H_{247}O_{61}N_{25}P$. As per this mean composition, the $r_{O_2:P}$ ratio is estimated to be –216,
497   which is ∼45% more negative than its present-day value of –150[64]. In other words, 45% more O_2
498   is consumed per mole of organic phosphorus liberated during organic matter remineralization.
499
500   As mentioned above, the majority of O_2 sinks on the present-day Earth were negligible during the
501   Neoproterozoic snowball Earth events. However, reducing volcanic emissions (SO_2, H_2S, CO,
502   CH_4, H_2) can be an important sink for O_2 in a globally glaciated climate (Table S2). All listed
503   fluxes are approximate but can be used to reasonably estimate the equivalent moles of O_2
504   consumed annually by oxidation of the reduced gases.

Methods references:

507   33.   Marshall, J., Adcroft, A., Hill, C., Perelman, L. & Heisey, C. A finite-volume,
508   incompressible Navier Stokes model for studies of the ocean on parallel computers. *J Geophys Res Oceans* **102**, 5753–5766 (1997).
510   34.   McDougall, T. J., Jackett, D. R., Wright, D. G. & Feistel, R. Accurate and Computationally Efficient Algorithms for Potential Temperature and Density of Seawater. *J Atmos Ocean Technol* **20**, 730–741 (2003).
513   35.   Redi, M. H. Oceanic Isopycnal Mixing by Coordinate Rotation. *J Phys Oceanogr* **12**, 1154–1158 (1982).
515   36.   Gent, P. R. & Mcwilliams, J. C. Isopycnal Mixing in Ocean Circulation Models. *J Phys Oceanogr* **20**, 150–155 (1990).
517   37.   Pollack, H. N., Hurter, S. J. & Johnson, J. R. Heat flow from the Earth's interior: Analysis of the global data set. *Reviews of Geophysics* **31**, 267–280 (1993).
519   38.   Valdes, P. J., Scotese, C. R. & Lunt, D. J. Deep ocean temperatures through time. *Climate of the Past* **17**, 1483–1506 (2021).
521   39.   Liu, Y., Peltier, W. R., Yang, J. & Vettoretti, G. The initiation of Neoproterozoic 'snowball' climates in CCSM3: The influence of paleocontinental configuration. *Climate of the Past* **9**, 2555–2577 (2013).
524   40.   Zhao, Z., Liu, Y. & Dai, H. Sea-glacier retreating rate and climate evolution during the marine deglaciation of a snowball Earth. *Glob Planet Change* **215**, 103877 (2022).
526   41.   Ashkenazy, Y. & Tziperman, E. A Wind-Induced Thermohaline Circulation Hysteresis and Millennial Variability Regimes. *J Phys Oceanogr* **37**, 2446–2457 (2007).
528   42.   Ashkenazy, Y. The surface temperature of Europa. *Heliyon* **5**, e01908 (2019).
529   43.   Ashkenazy, Y., Sayag, R. & Tziperman, E. Dynamics of the global meridional ice flow of Europa's icy shell. *Nat Astron* **2**, 43–49 (2018).
531   44.   Losch, M. Modeling ice shelf cavities in a *z* coordinate ocean general circulation model. *J Geophys Res* **113**, C08043 (2008).
533   45.   McKinley, G. A., Follows, M. J. & Marshall, J. Mechanisms of air-sea CO2 flux variability in the equatorial Pacific and the North Atlantic. *Global Biogeochem Cycles* **18**, 1–14 (2004).
536   46.   Dutkiewicz, S., Sokolov, A. P., Scott, J. & Stone, P. H. A three-dimensional ocean-seaice-carbon cycle model and its coupling to a two-dimensional atmospheric model: uses in climate change studies. *Joint Program Report Series Report* 47 (2005).

539   47.   Yamanaka, Y. & Tajika, E. Role of dissolved organic matter in the marine
540   biogeochemical cycle: Studies using an ocean biogeochemical general circulation model.
541   *Global Biogeochem Cycles* **11**, 599–612 (1997).

542   48.   Martin, J. H., Knauer, G. A., Karl, D. M. & Broenkow, W. W. VERTEX: carbon cycling
543   in the northeast Pacific. *Deep Sea Research Part A, Oceanographic Research Papers* **34**,
544   267–285 (1987).

545   49.   Halevy, I., Alesker, M., Schuster, E. M., Popovitz-Biro, R. & Feldman, Y. A key role for
546   green rust in the Precambrian oceans and the genesis of iron formations. *Nat Geosci* **10**,
547   135–139 (2017).

548   50.   Millero, F. J., Sotolongo, S. & Izaguirre, M. The oxidation kinetics of Fe(II) in seawater.
549   *Geochim Cosmochim Acta* **51**, 793–801 (1987).

550   51.   Komada, T. *et al.* Dissolved organic carbon dynamics in anaerobic sediments of the Santa
551   Monica Basin. *Geochim Cosmochim Acta* **110**, 253–273 (2013).

552   52.   Mottl, M. J. *et al.* Warm springs discovered on 3.5 Ma oceanic crust, eastern flank of the
553   Juan de Fuca Ridge. *Geology* **26**, 51–54 (1998).

554   53.   Elderfield, H. & Schultz, A. Mid-ocean ridge hydrothermal fluxes and the chemical
555   composition of the ocean. *Annu Rev Earth Planet Sci* **24**, 191–224 (1996).

556   54.   Halevy, I. & Bachan, A. The geologic history of seawater pH. *Science (1979)* **355**, 1069–
557   1071 (2017).

558   55.   Poulton, S. W. & Raiswell, R. The low-temperature geochemical cycle of iron: From
559   continental fluxes to marine sediment deposition. *Am J Sci* **302**, 774–805 (2002).

560   56.   Wolery, T. J. & Sleep, N. H. Hydrothermal Circulation and Geochemical Flux at Mid-
561   Ocean Ridges. *J Geol* **84**, 249–275 (1976).

562   57.   Hart, R. A. A Model for Chemical Exchange in the Basalt–Seawater System of Oceanic
563   Layer II. *Can J Earth Sci* **10**, 799–816 (1973).

564   58.   Thompson, K. J. *et al.* Photoferrotrophy, deposition of banded iron formations, and
565   methane production in Archean oceans. *Sci Adv* **5**, (2019).

566   59.   Korenaga, J. Archean Geodynamics and the Thermal Evolution of Earth. *Archean
567   Geodynamics and Environments* 7–32 Preprint at
568   https://doi.org/https://doi.org/10.1029/164GM03 (2006).

569   60.   Molina, E., Martínez, M. E., Sánchez, S., García, F. & Contreras, A. Growth and
570   biochemical composition with emphasis on the fatty acids of Tetraselmis sp. *Appl
571   Microbiol Biotechnol* **36**, 21–25 (1991).

572   61.   Fábregas, J., Patiño, M., Vecino, E., Cházaro, F. & Otero, A. Productivity and
573   biochemical composition of cyclostat cultures of the marine microalga Tetraselmis
574   suecica. *Appl Microbiol Biotechnol* **43**, 617–621 (1995).

575   62.   Tahiri, M., Benider, A., Belkoura, M. & Dauta, A. Caractérisation biochimique de l'algue
576   verte Scenedesmus abundans : influence des conditions de culture. *Annales de Limnologie
577   - International Journal of Limnology* **36**, 3–12 (2000).

578   63.   Viegas, C. V. *et al.* Algal products beyond lipids: Comprehensive characterization of
579   different products in direct saponification of green alga Chlorella sp. *Algal Res* **11**, 156–
580   164 (2015).

581   64.   Anderson, L. A. On the hydrogen and oxygen content of marine phytoplankton. *Deep Sea
582   Research Part I: Oceanographic Research Papers* **42**, 1675–1680 (1995).

583   65.   Sharoni, S. & Halevy, I. Geologic controls on phytoplankton elemental composition.
584   *Proceedings of the National Academy of Sciences* **119**, e2113263118 (2022).

585

Data and code availability:

The simulations are carried out using the MITgcm, an open-source ocean model that can be downloaded from: https://mitgcm.readthedocs.io/en/latest/overview/overview.html. The specific model configuration is available upon request.

Author contributions:

Conceptualization: KG, IH, HG, YA, ET

Data curation: KG

Formal Analysis: KG

Funding acquisition: HG, YA

Investigation: KG

Methodology: KG, IH, HG

Project administration: HG, YA

Resources: HG, YA

Software: KG, YA

Supervision: IH, HG, YA, ET

Validation: KG, IH, HG

Visualization: KG, IH, HG

Writing – original draft: KG, IH, HG, YA, ET

Competing interests:

Authors declare that they have no competing interests.

Supplementary Information:

Rate of Fe^{2+} oxidation during the Sturtian pan-glacial

To compare our model results with observations, we estimate the rate of Fe^{2+} oxidation (and Fe^{3+} deposition) during the Sturtian pan-glacial from BIFs dated to the glaciation using the following expression:

$$R_{Fe^{3+}} = n_{Fe} \times f_{Fe_2O_3} \times \rho_{BIF} \times \frac{h}{T_{deposition}},$$

622 where $n_{Fe} = 12.525$ is the number of moles of Fe in 1 kg of Fe_2O_3, $f_{Fe_2O_3}$ is the fraction of Fe_2O_3
623 in the BIF samples, ρ_{BIF} is the density of BIF in kg m^{-3}, and h and $T_{deposition}$ are the observed
624 thickness and the estimated depositional duration of the sampled BIF, respectively.
625
626 Iron formation and hematite mudstone samples obtained from diamond drill cores Y-5 and N-7 in
627 the Snake River deposit indicate that $f_{Fe_2O_3}$ in the two cores is 48.5% and 41.7% and the thickness
628 of the iron formation (estimated from the stratigraphic sections) is ~82 m and ~26 m,
629 respectively[16]. The estimated ρ_{BIF}, calculated by assuming that the non-iron-bearing-component
630 in BIFs has a density of 2,700 kg m^{-3}, for the two cores is 3,894 kg m^{-3} and 3,649 kg m^{-3}. The
631 Snake River deposit is a part of the Rapitan Group of glacial deposits. Another glacial unit of the
632 Rapitan Group is exposed along the Hard Luck Creek in the Tatonduk inlier. The iron formation
633 in this region is ~3 m thick[17] and the median $f_{Fe_2O_3}$ is 17.2%[25], which yields a ρ_{BIF} of 3,155 kg m^{-3}.
634 The Rapitan BIFs sit in the Sayunei formation that is under the Shezal formation. The transition
635 from the Sayunei to the Shezal formation is dated to 711.34±0.25 Ma[66]. Assuming that none of the
636 iron precipitated prior to the onset of the Sturtian pan-glacial (717±0.5 Ma; Ref. [10]) and that
637 deposition of other iron-poor facies in the formation (e.g., siltstone, sandstone) was rather rapid,
638 suggests that the Rapitan BIFs were deposited in 4.9–6.4 million years. The equation above, yields
639 $R_{Fe^{3+}}$ corresponding to the Rapitan BIFs that is between ~0.003 and ~0.4 mol m^{-2} y^{-1}.
640
641 The BIFs in the Kingston Peak Formation are ~28 m thick and have a median $f_{Fe_2O_3}$ of 50%[18],
642 which yields $\rho_{BIF} = 3,970$ kg m^{-3}. The upper Kingston Peak Formation that contains the BIFs is
643 correlated with the Wildrose submember[67], the depositional age of which has been constrained to
644 be between 705.4±0.3 and 645 Ma[8]. This suggests that the Kingston Peak Formation BIFs were
645 deposited over ~60 million years. However, we assume that duration of iron deposition did not
646 exceed the duration of the Sturtian pan-glacial, which yields $T_{deposition} = ~58$ million years[10]. Hence,
647 $R_{Fe^{3+}}$ for these IFs is constrained to ~0.01 mol m^{-2} y^{-1}.
648
649 Samples obtained from the Zhongjiajiang and Lanyang section of the Fulu Formation have a
650 median $f_{Fe_2O_3}$ of 19.6% and 24.2% and the maximum thickness of iron formation in the two
651 sections is ~22 m and ~50 m, respectively[19]. The estimated ρ_{BIF} for the two sections is 3,196 kg
652 m^{-3} and 3,313 kg m^{-3}. The maximum and minimum age of the Fulu formation is estimated to be
653 715.9±2.8 Ma and 691.9±8.0 Ma[19], which suggests that $T_{deposition}$ could have varied between 13.2
654 million years and 34.8 million years. Hence, $R_{Fe^{3+}}$ for the Fulu Formation is constrained to be
655 between ~0.005 and ~0.04 mol m^{-2} y^{-1}.
656
657 The Flinders Ranges in southern Australia house two more occurrences of BIFs, the Braemar and
658 the Holowilena Ironstones. The thickness of the Braemar Ironstone varies between ~24 m and ~76
659 m and the $f_{Fe_2O_3}$ is 58%[20], which yields a ρ_{BIF} of 4,192 kg m^{-3}. In contrast, stratigraphic sections
660 of the Holowilena Ironstone show that the thickness of banded hematite and jasper facies is
661 negligible and the formation predominantly comprises of ferruginous shale and diamictite[68]. We
662 estimate that the $T_{deposition}$ for these correlated formations[68] is between ~13.5 million years and 58
663 million years, based on the age of authigenic monazite from the upper part of the interglacial
664 succession [680±23 Ma, Ref. [69]] and the onset of the glaciation. Hence, $R_{Fe^{3+}}$ for the Australian
665 BIFs is constrained to between ~0.01 and ~0.2 mol m^{-2} y^{-1}.
666

667 Ironstone samples corresponding to the Chuos Formation obtained from the Mitten Fold locality
668 in the Damara Belt have a median $f_{Fe_2O_3}$ of 88.7% and the thickness of ironstone is ~25 m[21]. The
669 estimated ρ_{BIF} is 4,921 kg m^{-3}. Age constraints from geologic formations above and below the
670 Chuos Formation suggest that it was deposited between 760±1 Ma and 635±1 Ma[70,71], longer than
671 the duration of the Sturtian glaciation. Since the iron formation is syn-glacial, we adopt a
672 conservatively long $T_{deposition}$ of ~58 million years (the duration of the glaciation), yielding $R_{Fe^{3+}}$
673 of ~0.02 mol m^{-2} y^{-1}.

674

675 The above analysis suggests that the typical Fe^{3+} deposition rates during the Sturtian pan-glacial
676 were between ~0.003 and ~0.4 mol m^{-2} y^{-1}. This deposition rate is conservatively low, since in all
677 cases the BIFs deposited over a duration that is shorter than or equal to the duration of deposition
678 estimated from radiometric ages or from the duration of the Sturtian glaciation. We have excluded
679 the Jakkalsberg member of the Numees formation and the Tany formation from this analysis due
680 to difficulties in evaluating the thickness and Fe content of the Fe-rich parts of these two
681 formations.

682

Numerical simulations

684 While carrying out the simulations, we use asynchronous integration[72] with a momentum time step
685 of 1,800 seconds and a tracer (temperature and salinity) time step of 18,000 seconds to integrate
686 the primitive equations, to a quasi-steady state. Subsequently, the distribution of biogeochemical
687 variables was determined from the velocity fields and eddy diffusivities calculated from the
688 primitive equations. To calculate the distribution of biogeochemical variables, the integration time
689 step was set to 10,800 seconds. The results did not change with increasing temporal resolution,
690 indicating convergence.

691

Supplementary references:

693

694 66. Baldwin, G. J., Turner, E. C. & Kamber, B. S. Tectonic controls on distribution and
695   stratigraphy of the Cryogenian Rapitan iron formation, northwestern Canada.
696   *Precambrian Res* **278**, 303–322 (2016).
697 67. Macdonald, F. A. *et al.* The Laurentian record of Neoproterozoic glaciation, tectonism,
698   and eukaryotic evolution in Death Valley, California. *Geol Soc Am Bull* **125**, 1203–1223
699   (2013).
700 68. Lechte, M. A. & Wallace, M. W. Sedimentary and tectonic history of the Holowilena
701   Ironstone, a Neoproterozoic iron formation in South Australia. *Sediment Geol* **329**, 211–
702   224 (2015).
703 69. Mahan, K. H., Wernicke, B. P. & Jercinovic, M. J. Th–U–total Pb geochronology of
704   authigenic monazite in the Adelaide rift complex, South Australia, and implications for
705   the age of the type Sturtian and Marinoan glacial deposits. *Earth Planet Sci Lett* **289**, 76–
706   86 (2010).
707 70. Halverson, G. P., Hoffman, P. F., Schrag, D. P., Maloof, A. C. & Rice, A. H. N. Toward a
708   Neoproterozoic composite carbon-isotope record. *GSA Bulletin* **117**, 1181–1207 (2005).
709 71. Hoffmann, K.-H., Condon, D. J., Bowring, S. A. & Crowley, J. L. U-Pb zircon date from
710   the Neoproterozoic Ghaub Formation, Namibia: Constraints on Marinoan glaciation.
711   *Geology* **32**, 817–820 (2004).
712 72. Bryan, K. Accelerating the Convergence to Equilibrium of Ocean-Climate Models. *J Phys*
713   *Oceanogr* **14**, 666–673 (1984).

714 73. Arnold, R. G., Olson, T. M. & Hoffmann, M. R. Kinetics and mechanism of dissimilative
715 Fe(III) reduction byPseudomonas sp. 200. *Biotechnol Bioeng* **28**, 1657–1671 (1986).
716 74. Liu, C., Kota, S., Zachara, J. M., Fredrickson, J. K. & Brinkman, C. K. Kinetic analysis of
717 the bacterial reduction of goethite. *Environ Sci Technol* **35**, 2482–2490 (2001).
718 75. Bonneville, S., van Cappellen, P. & Behrends, T. Microbial reduction of iron(III)
719 oxyhydroxides: Effects of mineral solubility and availability. *Chem Geol* **212**, 255–268
720 (2004).
721 76. Kriest, I. & Oschlies, A. On the treatment of particulate organic matter sinking in large-
722 scale models of marine biogeochemical cycles. *Biogeosciences* **5**, 55–72 (2008).
723 77. Cadle, R. D. A comparison of volcanic with other fluxes of atmospheric trace gas
724 constituents. *Reviews of Geophysics* **18**, 746–752 (1980).
725 78. Mori, T. & Notsu, K. Remote CO, COS, CO2, SO2, HCl detection and temperature
726 estimation of volcanic gas. *Geophys Res Lett* **24**, 2047–2050 (1997).
727 79. Wardell, L. J., Kyle, P. R. & Chaffin, C. Carbon dioxide and carbon monoxide emission
728 rates from an alkaline intra-plate volcano: Mt. Erebus, Antarctica. *Journal of Volcanology*
729 *and Geothermal Research* **131**, 109–121 (2004).
730 80. Holland, H. D. Why the atmosphere became oxygenated: A proposal. *Geochim*
731 *Cosmochim Acta* **73**, 5241–5255 (2009).
732 81. Bjerrum, C. J. & Canfield, D. E. Ocean productivity before about 1.9 Gyr ago limited by
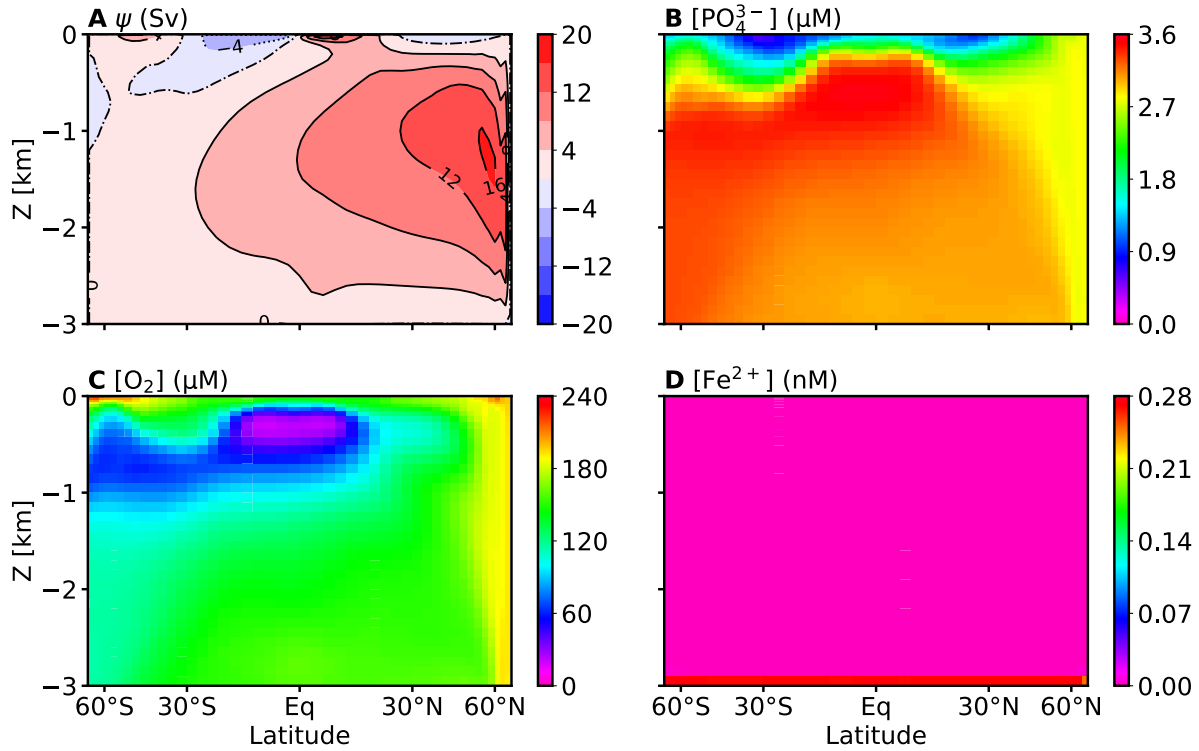733 phosphorus adsorption onto iron oxides. *Nature* **417**, 159–162 (2002).
734
735

Fig. S1. Results in box configuration simulation. (**A**) The meridional overturning circulation (1 Sv = 10^6 m^3 s^{-1}). The solid contours (streamlines) indicate clockwise circulation, the dotted contours indicate counterclockwise circulation and the dotted-dashed contours mark the zero values. Spatial distribution of (**B**) [PO$_4$$^{3-}$], (**C**) O$_2$ and (**D**) [Fe^{2+}]. The mean seawater [PO$_4$$^{3-}$] is 3.0 μM (100% modern) and stoichiometry of organic matter oxidation is $r_{O_2:P} = -150$, which is representative of the modern ocean.

736
737
738
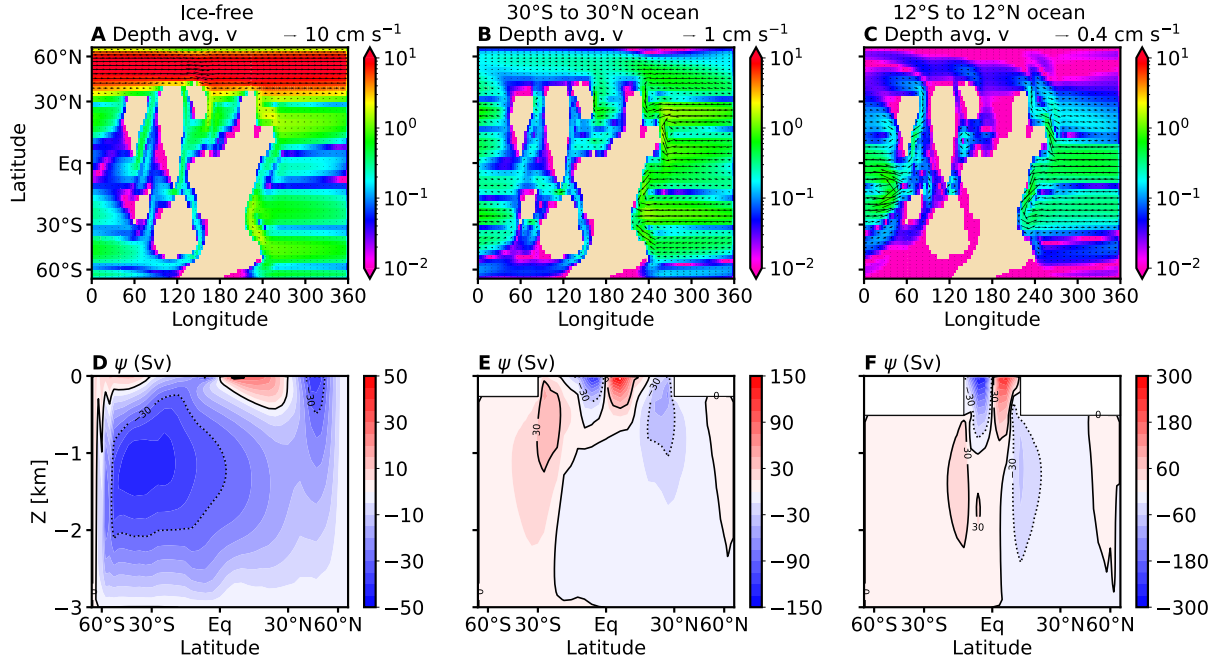
Fig. S2. Ocean circulation in the simulations for different meridional extent of ice-free region. Depth averaged velocity fields (the barotropic flow) and the meridional overturning circulation in the **(A)**,**(D)** ice-free simulations, and in the snowballs with ice-free ocean between **(B)**,**(E)** 30°S to 30°N ocean and **(C)**,**(F)** 12°S to 12°N. The colours in **(A)**-**(C)** denote the speed (cm s^{-1}) of the ocean currents. The solid contours (streamlines) in **(D)**-**(F)** indicate clockwise circulation, the dotted contours indicate counter clockwise circulation, and the dotted-dashed contours mark the zero values.
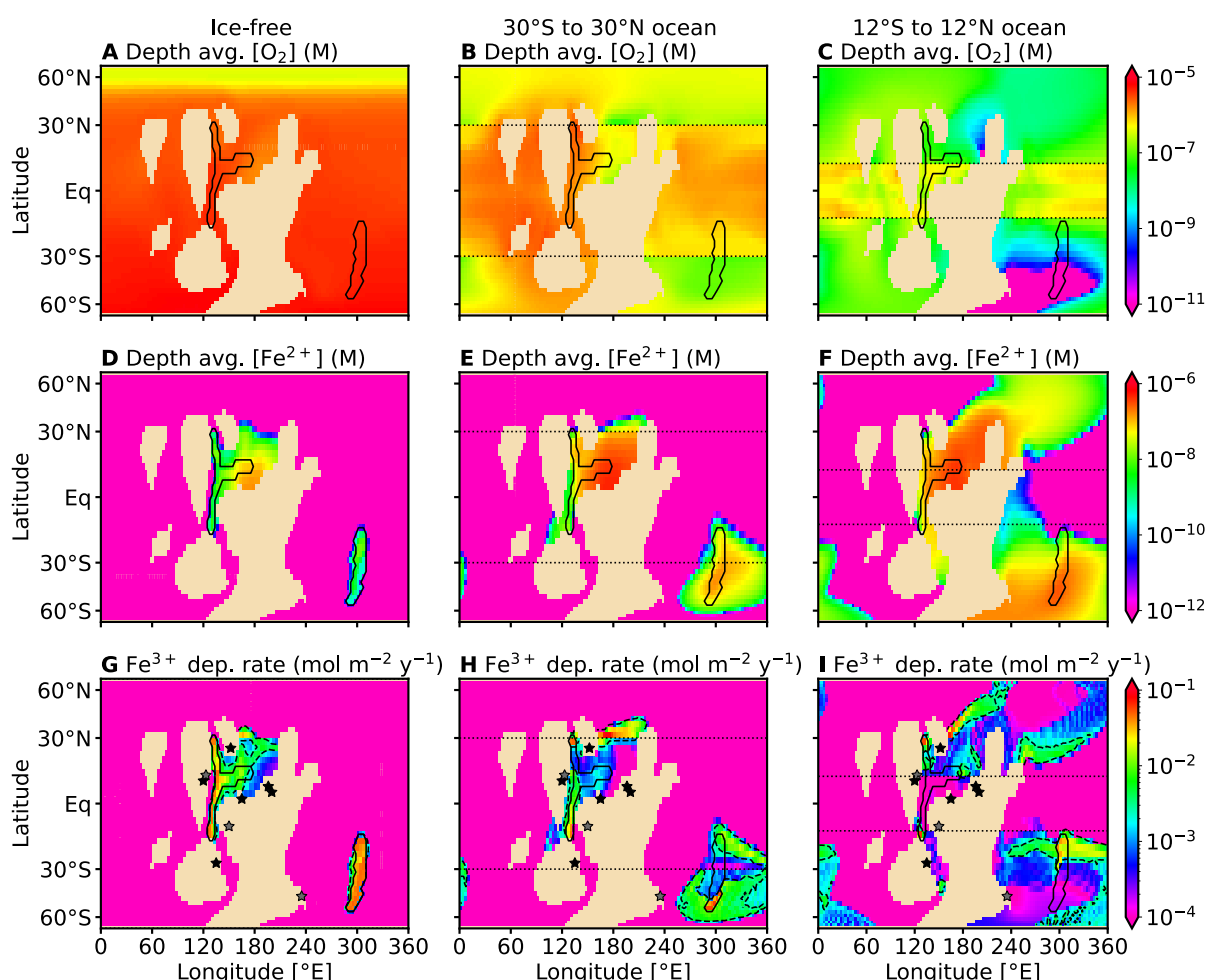
739
740

Fig. S3. Results of the 3D ocean model with a mean seawater [PO₄³⁻] of 0.03 μM (1% modern). (A)-(C) Depth-averaged distribution of [O$_2$] and (D)-(F) [Fe^{2+}] and the (G)-(I) spatial distribution of Fe^{3+} deposition rates in snowballs with different meridional extents of sea glaciers. The solid black contours mark the sites of hydrothermal Fe^{2+} injection, based on estimated locations of mid-oceanic ridges. The dotted black lines denote the extent of the ice-free region. The dashed black lines in (G)-(I) enclose the region where Fe^{3+} deposition rates are within the range estimated from Neoproterozoic BIFs. The stars indicate the approximate location of BIFs associated with the Sturtian pan-glacial. We note that for 1% modern [PO₄³⁻] levels, over 10% of the continental margins in the vicinity of Neoproterozoic BIFs are found to be appropriate for precipitation of BIFs, regardless of the extent of marine ice-cover. With ~21% of the margins under consideration viable for precipitation of BIFs, the ice-free ocean with 1% modern [PO₄³⁻] is in most agreement with the observed distribution of BIFs, followed by ~18% and ~13% in the 30°S to 30°N and 12°S to 12°N ocean, respectively. While an enhanced adsorption of PO₄³⁻ on iron oxides in an anoxic environment[81] can explain the concurrence between the model results for an ice-free ocean with 1% modern [PO₄³⁻] and the distribution of Neoproterozoic BIFs, the precipitation of BIFs in an ice-free ocean is inconsistent with other geochemical evidence that point towards a global glaciation during the Neoproterozoic[10].
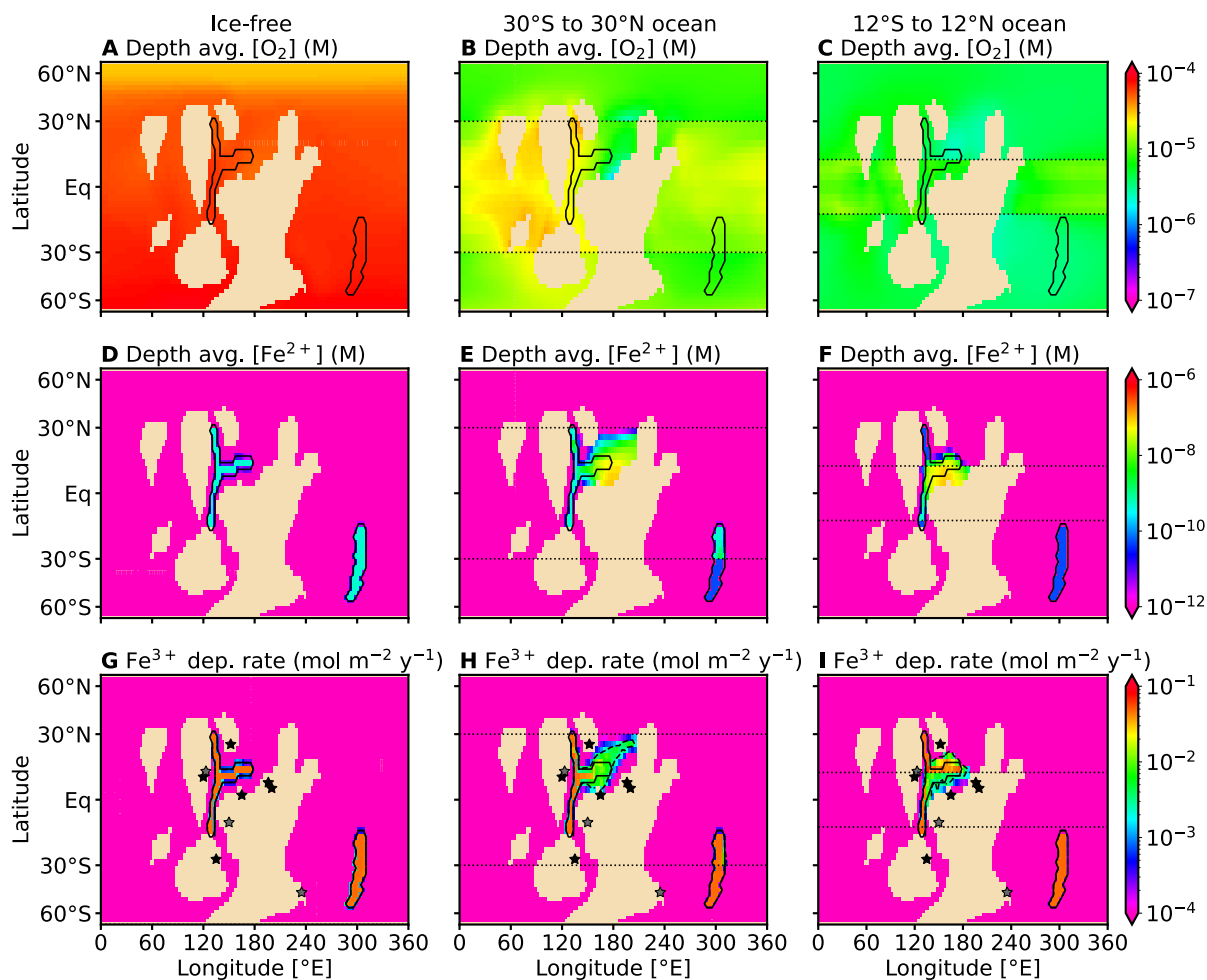
741

Fig. S4. Results of the 3D ocean model with a mean seawater [PO$_4^{3-}$] of 0.3 μM (10% modern). See Fig. S3 for the details regarding the different panels.

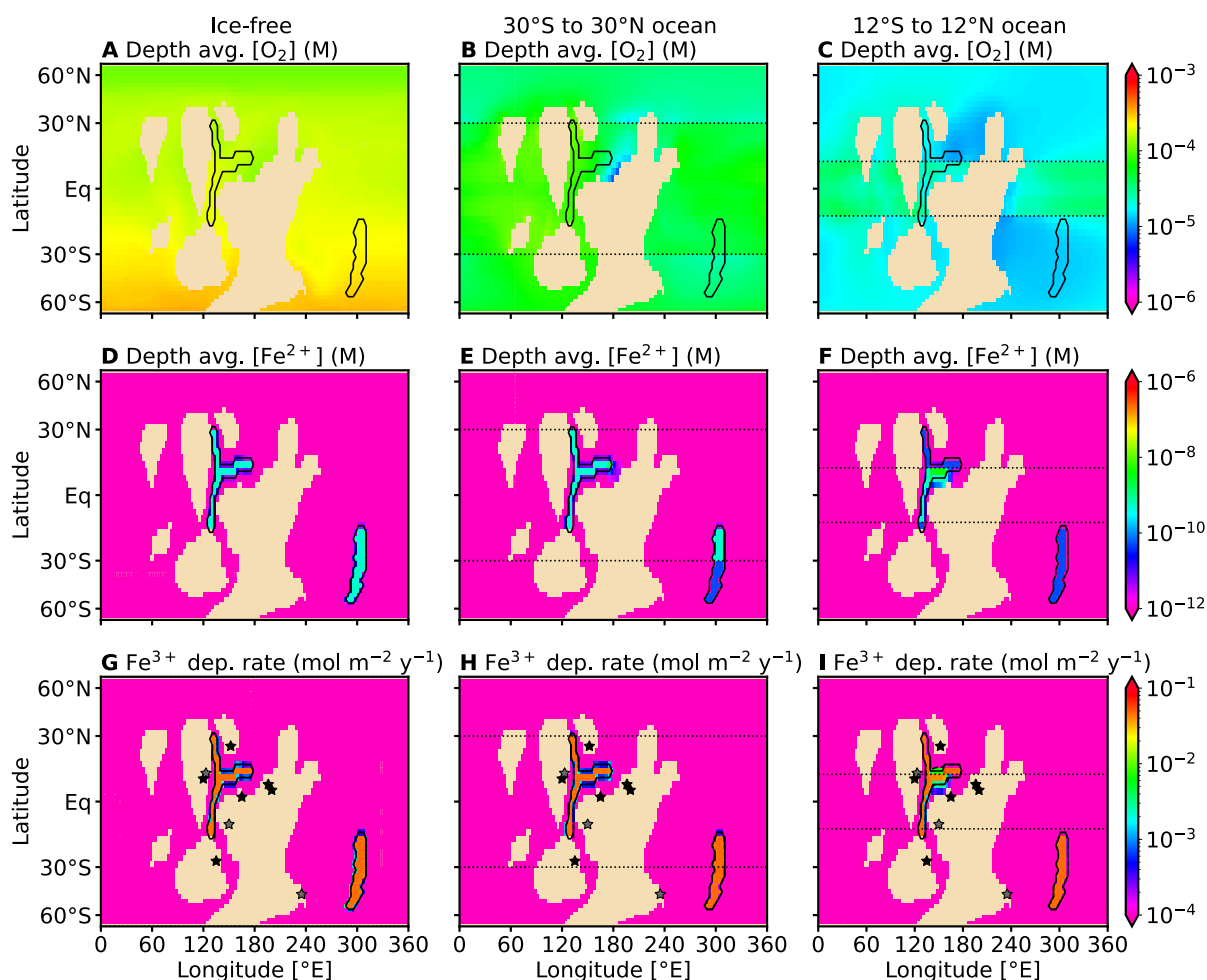**Fig. S5. Results of the 3D ocean model with a mean seawater [PO₄³⁻] of 3 µM (100% modern).** See Fig. S3 for the details regarding the different panels.
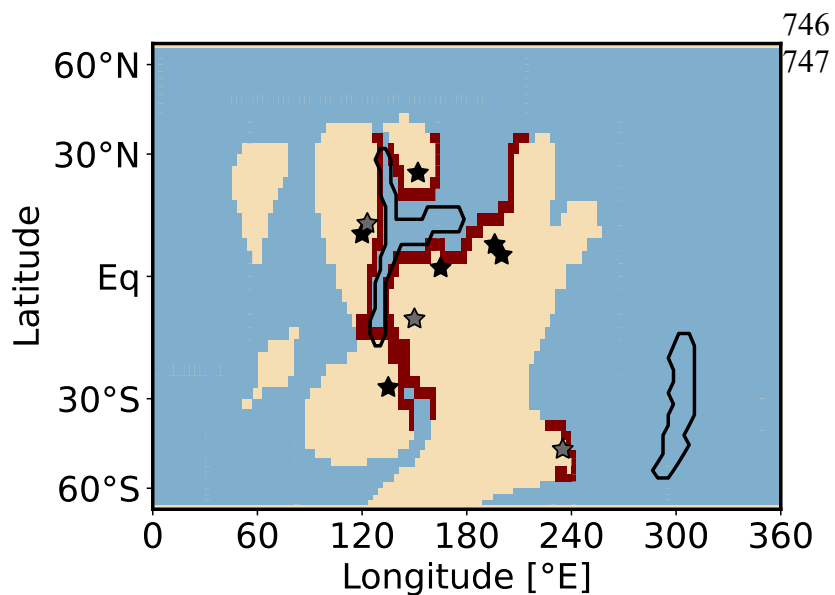
745

Fig. S6. Continental margins (brown) close to observed BIFs. The fraction of these margins where model Fe deposition occurred at rates between 0.003 and 0.4 mol m^{-2} y^{-1} was calculated to evaluate model-observation agreement. The solid black contours mark the sites of hydrothermal Fe^{2+} injection, based on estimated locations of mid-oceanic ridges. The stars indicate the approximate location of BIFs associated with the Sturtian pan-glacial.
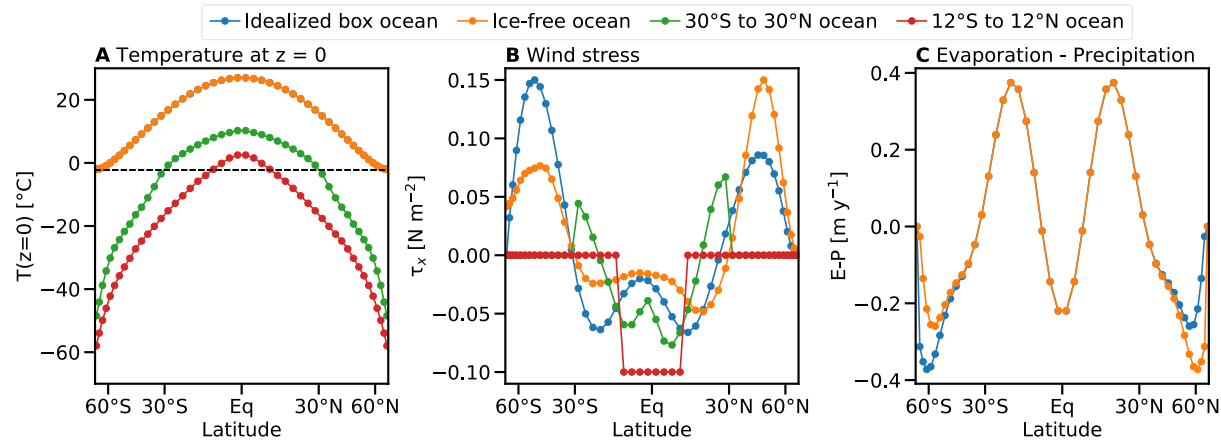
Fig. S7. Forcing (zonal-mean) over the ocean model. (**A**) Temperature forcing at z = 0 for the different meridional extent of sea glaciers. The temperature forcing in the idealized box configuration simulations and in the ice-free Neoproterozoic ocean is the same and the temperature forcing over the two snowballs has been adjusted to account for the fraction of the sea glacier floating above the sea surface. The black dashed line denotes the freezing temperature of seawater at salinity of 40.7 g/kg. (**B**) Wind stress applied over the ocean surface. The wind over the surface of the sea glaciers in the snowball simulations does not affect the ocean currents and thus is set to zero. (**C**) Evaporation minus Precipitation (E–P) fields over the ocean's surface in the box configuration simulations and in the ice-free ocean simulations. The slight asymmetry at the high latitudes is added to avoid small oscillations in overturning circulation. To conserve the salinity of the partially ice-covered oceans we do not prescribe an E–P field; instead the freshwater flux due to melting under the ice-shelves is balanced by evaporation in the ice-free region.
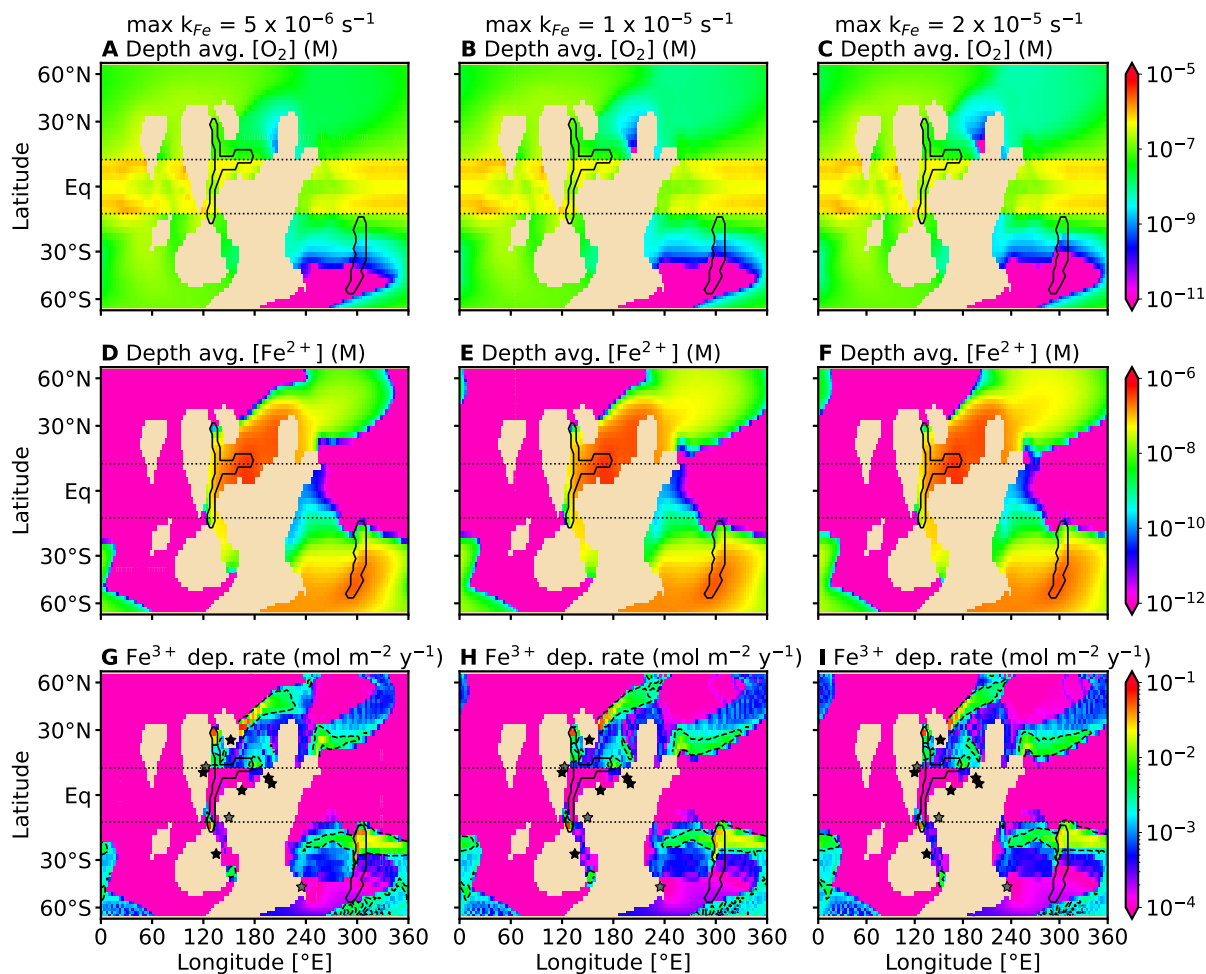
749
750

Fig. S8. Summary of profiles for sensitivity to maximum k_{Fe}. (**A**)-(**C**) and (**D**)-(**F**) show the depth averaged distribution of [O_2] and [Fe^{2+}] for maximum k_{Fe} = 5×10^{-6} s^{-1}, 1×10^{-5} s^{-1} and 2×10^{-5} s^{-1} respectively. (**G**)-(**I**) show the deposition rates, calculated by vertical integration of net Fe^{2+} oxidation profiles for the three values of maximum k_{Fe}. In all simulations shown, the ice-free ocean extends from 12°S to 12°N and the mean seawater [PO_4^{3-}] is 0.03 μM (1% modern).

751
752
753
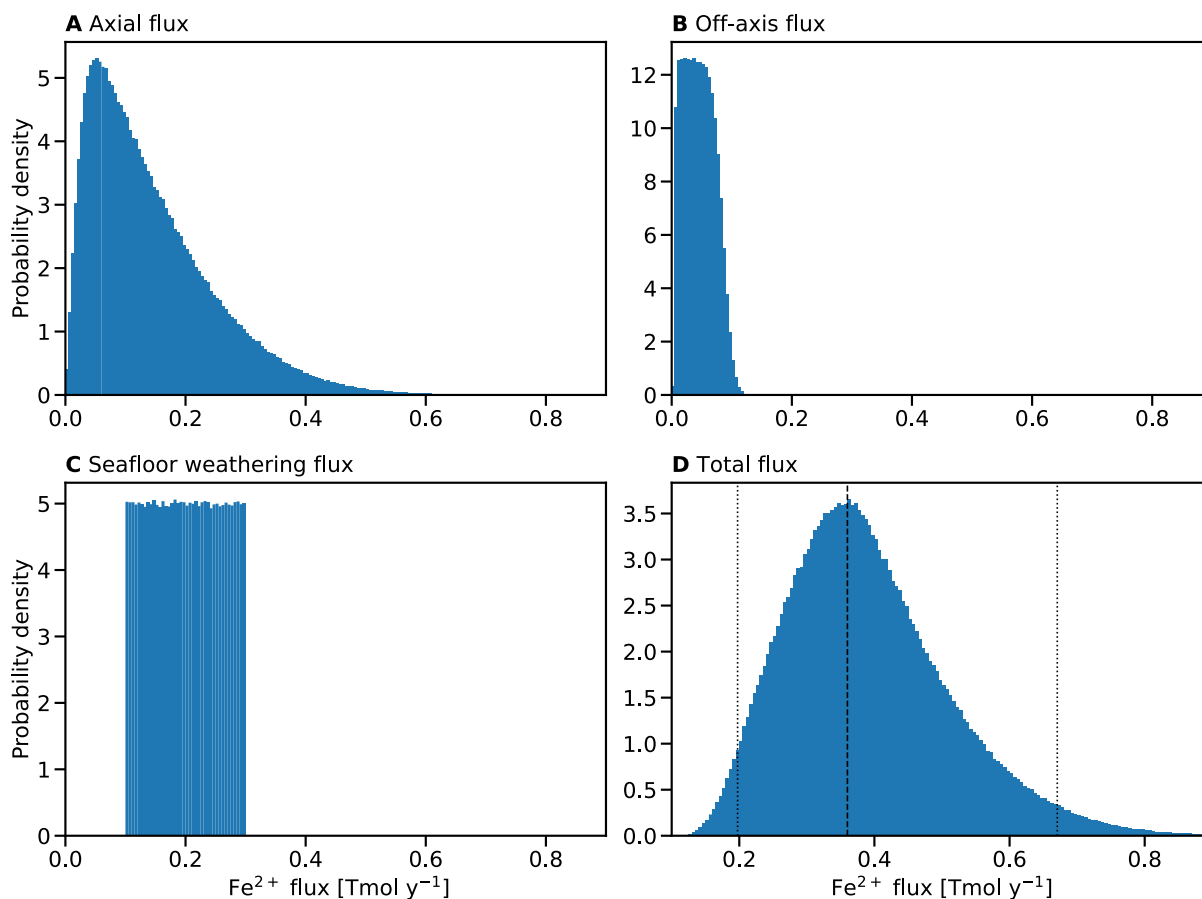754

Fig. S9. Probability distribution of estimated Fe²⁺ into the ocean from different sources. (**A**)-(**B**) The distribution of axial and off-axis flux of Fe^{2+} from hydrothermal ridges is calculated by assuming that the estimated values of axial and off-axis $[Fe^{2+}]$ are uniformly distributed and multiplying them with the respective distribution of sea-water flux[54]. (**C**) The Fe^{2+} influx from seafloor basalt weathering is assumed to be uniformly distributed between its estimated values[57]. (**D**) The distribution of total Fe^{2+} influx is calculated by convolving the three distributions shown in (**A**)-(**C**). The dotted lines denote the 95% confidence interval (0.2 to 0.67 Tmol y⁻¹) and the dashed line marks the mode value (0.36 Tmol y⁻¹).

755

Parameter	Symbol	Value	Units	References
Maximum community production	α	3×10^{-3}	mol P m^{-3} y^{-1}	[46]
Light half-saturation constant	κ_L	30	W m^{-2}	
Phosphate half-saturation constant	κ_{PO_4}	5×10^{-4}	mol P m^{-3}	
Fraction of SW radiation available for photosynthesis	f_{PAR}	0.4		
Light attenuation constant	k	0.02	m^{-1}	
Semi-labile consumption rate constant for DOP to PO$_4^{3-}$ remineralization	κ_{remin}	0.5	y^{-1}	
Fraction of PO$_4^{3-}$ converted to DOP via production	f_{DOP}	0.7		
Compensation depth	z_c	500	m	
Power law coefficient for POP remineralization	a_{remin}	0.9		
Moles of O$_2$ consumed per mole of P released by remineralization of typical Neoproterozoic marine biomass	$-r_{O_2:P}$	216		This study
Typical Fe^{3+} turnover rate due to anoxic bacterial respiration	μ	100	mol Fe m^{-3} y^{-1}	[73–75]
Organic matter half-saturation constant for anoxic bacterial respiration	κ_C	0.5	mol C m^{-3}	[74]
Iron half-saturation constant for anoxic bacterial respiration	κ_{Fe}	5	mol Fe m^{-3}	[75]
Vertical gradient of particle sinking velocity	a	12.6	y^{-1}	[76]
Fraction of Fe^{3+} preserved during anoxic bacterial respiration	$f_{preserved}$	0.1		This study
Mole equivalent rate of O$_2$ consumption to balance the flux of reduced gases into the atmosphere.	Φ_{red}	1.0	T mol y^{-1}	This study

758 **Table S1. Parameters of the biogeochemical model.**

759

Gas	Annual flux (T mol y^{-1})	O_2 flux required for oxidation (T mol y^{-1})
SO_2	0.30	0.30
H_2S	0.18	0.27
CO	0.06	0.03
CH_4	0.05	0.1
H_2	0.03	0.015

762 **Table S2. Volcanic flux of reducing gases.** Studies indicate that the $CO:CO_2$ ratio for volcanic
763 emissions is between 10^{-3} and 10^{-1} [77–79], and the flux of CO stated in Table S1 is calculated from
764 the flux of CO_2 estimated in Ref. [80] multiplied by the higher end of this range of ratios.

Iron formation	Age	$T_{deposition}$ (million years)	h (m)	Fe_2O_3 (% wt.)	ρ_{BIF} (kg m^{-3})	$R_{Fe^{3+}}$ (mol m^{-2} y^{-1})
Core Y5, Snake River deposit, Rapitan BIF	717 $\pm$ 0.5 Ma to 711.34 $\pm$ 0.25 Ma [10,66]	4.9 – 6.4	81.9 [16]	48.5 [16]	3894.4	0.3 – 0.4
Core N7, Snake River deposit, Rapitan BIF	717 $\pm$ 0.5 Ma to 711.34 $\pm$ 0.25 Ma [10,66]	4.9 – 6.4	25.9 [16]	41.7 [16]	3648.7	0.08 – 0.1
T709, Hard Luck Creek, Tatonduk BIF	717 $\pm$ 0.5 Ma to 711.34 $\pm$ 0.25 Ma [10,66]	4.9 – 6.4	2.7 [17]	17.2 [25]	3155.2	0.003 – 0.004
Section C-C', Kingston Range, Kingston Peak BIF	705.4 $\pm$ 0.3 Ma to 645 Ma [8,10]	58	27.6 [18]	49.6 [18]	3969.5	0.01
Zhongjiajiang section, Fulu BIF	715.9 $\pm$ 2.8 Ma to 691.9 $\pm$ 8.0 Ma [19]	13.2 – 34.8	21.9 [19]	19.6 [19]	3195.8	0.005 – 0.01
Lanyang section, Fulu BIF	715.9 $\pm$ 2.8 Ma to 691.9 $\pm$ 8.0 Ma [19]	13.2 – 34.8	50.4 [19]	24.2 [19]	3312.8	0.01 – 0.04
BR52, BR53, Braemar Ironstone	717 $\pm$ 0.5 Ma to 680 $\pm$ 23 Ma [10,69]	13.5 – 58	24.2 – 76.1 [20]	58 [20]	4199.7	0.01 – 0.2
Mitten Fold, Chuos BIF	760 $\pm$ 1 Ma to 635 $\pm$ 1 Ma [70,71]	58	25.1 [21]	88.7 [21]	4920.8	0.02

Table S3. Summary of Fe^{3+} deposition rates estimated from Sturtian BIFs. The approximate deposition duration corresponding to the formation, based on the difference in ages of the deposits above and below the formation, is given by $T_{deposition}$. If the difference is greater than the duration of the Sturtian glaciation, we assume that the deposition duration is equal to the glaciation duration. The thickness of BIFs, given by h, is calculated from the thickness of layered ironstone in the stratigraphic sections. The fraction of Fe_2O_3 in the BIF samples is used to estimate the density ρ_{BIF}. The Fe^{3+} deposition rate is determined using the formula discussed in the text.